International Journal of Solids and Structures 122–123 (2017) 42–58

Contents lists available at ScienceDirect

International Journal of Solids and Structures

journal homepage: www.elsevier.com/locate/ijsolstr

A new staggered algorithm for thermomechanical coupled problems

J.M.P. Martins[a,*], D.M. Neto[a], J.L. Alves[b], M.C. Oliveira[a], H. Laurent[c], A. Andrade-Campos[d], L.F. Menezes[a]

[a] CEMMPRE, Department of Mechanical Engineering, University of Coimbra, Polo II, Rua Luís Reis Santos, Pinhal de Marrocos, 3030-788 Coimbra, Portugal
[b] CMEMS, Microelectromechanical Systems Research Unit, University of Minho, Campus de Azurém, 4800-058 Guimarães, Portugal
[c] Univ. Bretagne Sud, FRE CNRS 3744, IRDL, F-56100 Lorient, France
[d] Department of Mechanical Engineering, Centre for Mechanical Technology and Automation, Grids, University of Aveiro, Campus Universitário de Santiago, 3810-193 Aveiro, Portugal

ARTICLE INFO

Article history:
Received 3 November 2016
Revised 5 May 2017
Available online 6 June 2017

Keywords:
Finite element method
Thermomechanical coupling
Staggered algorithm
Isothermal split
DD3IMP

ABSTRACT

This study presents a new staggered coupled strategy to deal with thermomechanical problems. The proposed strategy is based on the isothermal split methodology, i.e. the mechanical problem is solved at constant temperature and the thermal problem is solved for a fixed configuration. Nevertheless, the procedure for this strategy is divided into two phases within each increment: the prediction and the correction phases, while the interchange of information is performed on both. This allows taking advantage of automatic time-step control techniques, previously implemented for the mechanical problem, which is the main feature that distinguishes it from the classical strategies. The aim of the proposed strategy is to reduce the computational cost without compromising the accuracy of the results. The new coupling strategy is validated using three numerical examples, comparing its accuracy and performance with the ones obtained with the classical (commonly employed) strategies for solving thermomechanical problems. Moreover, the influence of the time-step size on the accuracy is analysed. The results indicate that the proposed strategy presents accuracy close to the one obtained with the implicit coupling algorithm, while the computational cost is only slightly higher than the one required by the explicit strategy.

1. Introduction

The analysis of thermomechanical coupled problems is of crucial interest in many engineering applications. These problems arise in several manufacturing processes, where the temperature is strategically used as a process parameter as, for example, welding processes (Rahman Chukkan et al., 2015), machining processes (Akbari et al., 2016) and hot/warm metal forming processes (Karbasian and Tekkaya, 2010; Laurent et al., 2015). In the welding and machining processes the temperature field influences the residual stresses and the part distortion and, consequently, its knowledge helps determining the process parameters. In the hot/warm metal forming manufacturing process, the blank temperature is increased to achieve better formability and reduce the springback effect (Neugebauer et al., 2006). On the other hand, the recent trend in the automotive industry of using advanced high strength steels changes the typical cold forming conditions, i.e. due to the substantial heat generated by plastic deformation there is a significant increase in the temperature conditions of the process, which is not intentional (Li et al., 2016; Pereira and Rolfe, 2014). Thus, in both situations, the influence of the thermal field on the mechanical field needs to be considered. This requires improved knowledge concerning heat transfer (conduction, convection and radiation), the heat generation (by plastic deformation and/or frictional sliding), the temperature dependence on the mechanical behaviour and the thermal expansion, which are some of coupling effects that play an important role in the interdependence between temperature and stress fields.

The finite element method (FEM) has become an increasingly important tool in the analyses of thermomechanical problems. Since the pioneering work of (Argyris et al., 1981), a large effort has been carried out towards efficient and robust solutions for this type of problems (Armero and J. C. Simo, 1992; Dunić et al., 2016; Felippa et al., 2001; Rothe et al., 2015). Nevertheless, the development of numerical algorithms to deal with the thermomechanical coupling remains a challenge due to the strong non-linearity of both problems. Furthermore, the industrial requirements for re-

* Corresponding author.
E-mail addresses: joao.pmartins@dem.uc.pt, joao_martins_52@hotmail.com (J.M.P. Martins), diogo.neto@dem.uc.pt (D.M. Neto), jlalves@dem.uminho.pt (J.L. Alves), marta.oliveira@dem.uc.pt (M.C. Oliveira), herve.laurent@univ-ubs.fr (H. Laurent), gilac@ua.pt (A. Andrade-Campos), luis.menezes@dem.uc.pt (L.F. Menezes).

http://dx.doi.org/10.1016/j.ijsolstr.2017.06.002
0020-7683/

liable and accurate solutions at lower computational cost demand new numerical strategies and algorithms.

The numerical treatment of thermomechanical problems can be carried out using two different approaches: the monolithic approach and the staggered approach (Armero and Simo, 1992; Danowski et al., 2013; Dunić et al., 2016; Rothe et al., 2015). In the monolithic approach, the mechanical and the thermal problems are solved simultaneously in each increment. The main advantage of this approach is the unconditional stability (Netz and Hartmann, 2015). Nevertheless, it has disadvantages, such as the fact that the resulting system of equations is usually non-symmetric (involving both displacements and temperatures), which requires a large computational time for its resolution (Novascone et al., 2015), and its numerical implementation requires the development of new code dedicated to thermomechanical problems, which is difficult to maintain (Cervera et al., 1996; Dunić et al., 2016). On the other hand, in the staggered approach, the global thermomechanical problem is split in two sub-problems (mechanical and thermal). Thus, the outcome of this approach are two smaller systems of equations in each increment, one for each sub-problem (Felippa et al., 2001). Moreover, this approach allows to use different time scales and spatial discretizations for each sub-problem (Armero and J. C. Simo, 1992; Danowski et al., 2013). Its finite element implementation is very flexible in comparison with the monolithic approach, enabling to reuse finite element codes already developed for each sub-problem (Cervera et al., 1996; Dunić et al., 2016).

Regarding the staggered approach, the thermomechanical coupling can be carried out following one of two methodologies. The standard methodology is the so-called isothermal split, where the global thermomechanical problem is split into a mechanical problem solved at constant temperature and a thermal problem solved for a fixed configuration (Argyris and Doltsinis, 1981). The main drawback of this methodology is the conditional stability, which arises when the thermoelastic effects play an important role. On the other hand, the so-called adiabatic split methodology, proposed by Armero and Simo (Armero and Simo, 1992), avoids the stability problem, retaining the property of unconditional stability of the monolithic approach. In this case, the global thermomechanical problem is split into a mechanical problem solved at constant entropy, followed by a thermal problem solved for a fixed configuration. Despite this methodology being adopted in several works (Agelet De Saracibar et al., 1999; Ulz, 2009), the stability problem of the isothermal split is not really an issue for classical materials used in metal forming (Adam and Ponthot, 2002; Canadija and Brnic, 2004; Håkansson et al., 2005). This aspect was discussed by Armero and Simo (1993) and Agelet De Saracibar et al. (1999), concluding that the value of the thermal expansion coefficient needs to be unrealistically high to obtain unstable results in the isothermal split. Accordingly, many commercial and non-commercial finite element codes resort to the isothermal split, which is adopted also in this study.

Within the class of isothermal split algorithms, the development of new algorithms with improved accuracy and lower computational cost is still an area of interest, in order to be efficiently applied in industrial applications. In this context, (Erbts and Düster, 2012) presented the design of an implicit coupling algorithm, testing different strategies to accelerate convergence. The main objective of the authors was to model an innovative technology called Field Assisted Sintering Technology. Lee et al. (Lee et al., 2015) presented an explicit coupling algorithm for the analysis of a forming process of a dual-phase steel exposed to infrared local heating. It should be noted that this type of algorithms, implicit and explicit, are the most common. The implicit algorithms have the main advantage of ensuring higher accuracy on the results, whereas the explicit algorithms are developed for reach a low computational cost, sometimes at the expense of accuracy. Accordingly, the aim of this work is to propose a new solution for the thermomechanical coupling based on a staggered approach and following an isothermal split methodology. The proposed algorithm was designed to reduce the computational cost without compromising the accuracy of the results, through a modified explicit approach.

This work constitutes the first part of a project which aims to develop an efficient and robust dedicated finite element code for the numerical simulation of warm sheet metal forming process. This finite element code will enable an evaluation of the technological process parameters affecting the warm sheet metal forming and, consequently, contribute to the knowledge, development and dissemination of this technology. Thus, the new algorithm was implemented in the in-house finite element code DD3IMP (Menezes and Teodosiu, 2000; Oliveira et al., 2008), which was initially developed to simulate isothermal sheet metal forming processes. Since the focus of this work is the analysis and validation of the coupling algorithms, both the examples and constitutive models adopted in the present study are simple to focus the attention on the thermomechanical coupling approach.

The outline of the paper is as follows. Section 2 starts with a brief introduction of the formulation behind the thermomechanical problem. Section 3 presents the classical coupling (explicit and implicit) algorithms and a detailed description of the proposed algorithm. In Section 4, three numerical examples are studied, validating the proposed algorithm and assessing its accuracy and performance. Section 5 closes the paper discussing the main conclusions.

2. Formulation of the thermomechanical problem

2.1. Mechanical model

Since the algorithms related with the mechanical problem were already implemented in the in-house finite element code DD3IMP (Menezes and Teodosiu, 2000), a short description of this mechanical formulation is given. The mechanical problem is assumed *quasi*-static, adopting an hypoelastic law for the material behaviour description, while the evolution of the deformation process is described by an updated Lagrangian formulation. Regarding the algorithm used for solving the mechanical problem, an explicit approach is used to determine a trial solution, which is adjusted by the $r_{\min}$ strategy, an automatic time-step control technique to restrict the increment size (Oliveira and Menezes, 2004; Yamada et al., 1968). This strategy is used to improve the convergence rate of the iterative Newton-Raphson algorithm adopted in the implicit approach, which corrects the trial solution until the equilibrium state is achieved.

Although the frictional contact is important in the modelling of sheet metal forming processes (Neto et al., 2016, 2015), this study is focused in the thermoelastoplastic problem with large strains and rotations, neglecting the frictional contact conditions.

2.1.1. Kinematics for large deformation continuum mechanics

Consider that $\mathcal{B}$ is a continuum body with domain defined in the three-dimensional Euclidean space $\mathbb{R}^3$. It is assumed that $\mathcal{B}$ is a continuous set of particles defined by spatial points. At the time t_0, the continuum body occupies a region in space, C_0, called reference configuration, where the position of a generic point $\wp$ is defined by the position vector $\mathbf{x}_0$. Suppose body $\mathcal{B}$, at the time instant t, assumes another configuration, C, called the current configuration, where the position of the same generic point $\wp$ is defined by the position vector $\mathbf{x}$.

The evolution of this point's position is defined by a smooth one-to-one function, called deformation mapping, represented by

$$\mathbf{x} = \varphi(\mathbf{x}_0, t), \tag{1}$$

thus, the displacement vector, between the two instants t_0 and t, can be defined as

$$\mathbf{u} = \mathbf{u}(\mathbf{x}_0, t) = \varphi(\mathbf{x}_0, t) - \mathbf{x}_0. \tag{2}$$

Consequently, the displacement rate, or velocity, associated to the motion of the point $\wp$ at instant t is defined as

$$\mathbf{v} = \dot{\mathbf{x}}(\mathbf{x}_0, t) = \frac{\partial \mathbf{x}(\mathbf{x}_0, t)}{\partial t}. \tag{3}$$

The key quantity in finite deformation is the deformation gradient, which corresponds to the finite transformation between the position $\mathbf{x}_0$ and $\mathbf{x}$, and is defined by

$$\mathbf{F}(\mathbf{x}_0, t) = \frac{\partial}{\partial \mathbf{x}_0}\mathbf{x}(\mathbf{x}_0, t), \text{ with } \det(\mathbf{F}) > 0. \tag{4}$$

The theorem of polar decomposition states that the deformation gradient can be decomposed as

$$\mathbf{F}(\mathbf{x}_0, t) = \mathbf{RU}. \tag{5}$$

where $\mathbf{R}$ is the orthogonal rotation tensor and $\mathbf{U}$ is the right symmetric stretch tensor.

The spatial velocity gradient corresponding to (3) is given by

$$\mathbf{L}(\mathbf{x}, t) = \frac{\partial}{\partial \mathbf{x}}\mathbf{v}(\mathbf{x}, t) = \dot{\mathbf{F}}\mathbf{F}^{-1}, \tag{6}$$

where $\dot{\mathbf{F}}$ is the time derivative of the deformation gradient. The velocity gradient can be decomposed in a symmetric and antisymmetric part. The symmetric part is called the deformation rate tensor $\mathbf{D}$ and the antisymmetric part is the spin rate tensor $\mathbf{W}$. These can be defined as

$$\mathbf{D}(\mathbf{x}, t) = \frac{1}{2}\left(\mathbf{L} + \mathbf{L}^{\mathrm{T}}\right) \tag{7}$$

and

$$\mathbf{W}(\mathbf{x}, t) = \frac{1}{2}\left(\mathbf{L} - \mathbf{L}^{\mathrm{T}}\right). \tag{8}$$

2.1.2. Constitutive model

As mentioned earlier, the hypoelastic stress-strain relation is adopted for the description of the material behaviour. Based on that, the formulation of the Hooke's law can be written as

$$\dot{\boldsymbol{\sigma}}^{\mathrm{J}} = \mathbf{C}^{\mathrm{e}} : \mathbf{D}^{\mathrm{e}}, \tag{9}$$

where $\dot{\boldsymbol{\sigma}}^{\mathrm{J}}$ is the Jaumann derivative of the Cauchy stress tensor $\boldsymbol{\sigma}$, chosen in order to satisfy the objectivity condition, and defined as

$$\dot{\boldsymbol{\sigma}}^{\mathrm{J}} = \dot{\boldsymbol{\sigma}} + \boldsymbol{\sigma}W - \mathbf{W}\sigma, \tag{10}$$

where $\dot{\boldsymbol{\sigma}}$ is the time derivative of the Cauchy stress tensor. Although omitted to simplify the notation, the remaining tensors in Eq. (9) are assumed to turn with the spin tensor, thus corresponding to the Jaumman derivative. However, as the elastic behaviour is assumed linear isotropic, the fourth-order tensor of elastic constants $\mathbf{C}^{\mathrm{e}}$ is invariant with the rotation and is given by

$$\mathbf{C}^{\mathrm{e}}(T) = \mu(T)\left(\mathbf{I}_4 + \mathbf{I}_4^{\mathrm{T}}\right) + \lambda(T)\mathbf{I} \otimes \mathbf{I}, \tag{11}$$

where $\mathbf{I}$ is the second-order identity tensor and $\mathbf{I}_4$ is the fourth-order identity tensor. In order to be consistent with a thermoelastic formulation, the fourth-order tensor of elastic constants is assumed temperature-dependent, so $\lambda(T)$ and $\mu(T)$ are the temperature-dependent Lamé coefficients (Ponthot and Papeleux, 2014).

In the case of thermoelastoplastic problems, the additive decomposition of the strain rate tensor is usually assumed (Adam and Ponthot, 2005; Andrade-Campos et al., 2007; Xing and Makinouchi, 2002b), which can be presented as

$$\mathbf{D} = \mathbf{D}^{\mathrm{e}} + \mathbf{D}^{\mathrm{th}} + \mathbf{D}^{\mathrm{p}}, \tag{12}$$

where $\mathbf{D}^{\mathrm{e}}$, $\mathbf{D}^{\mathrm{th}}$ and $\mathbf{D}^{\mathrm{p}}$ are the elastic, the thermal and the inelastic (or plastic) strain rate contributions, respectively. The thermal strain rate tensor enables to model the volumetric thermal contribution to the total strain and can be defined as

$$\mathbf{D}^{\mathrm{th}} = \alpha_T^*(T)\dot{T}\mathbf{I} \tag{13}$$

with

$$\alpha_T^*(T) = \alpha_T(T) + \frac{\partial \alpha_T(T)}{\partial T}(T - T_{\mathrm{ref}}), \tag{14}$$

where $\alpha_T(T)$ is the thermal expansion coefficient and T and $\dot{T}$ are the temperature and the time derivative of the temperature, respectively (Andrade-Campos et al., 2007; Xing and Makinouchi, 2002b).

From Eq. (12), the hypoelastic formulation of the Hooke's law assumes the following form

$$\dot{\boldsymbol{\sigma}}^{\mathrm{J}} = \mathbf{C}^{\mathrm{e}}(T) : \left(\mathbf{D} - \mathbf{D}^{\mathrm{th}} - \mathbf{D}^{\mathrm{p}}\right) + \frac{\partial \mathbf{C}^{\mathrm{e}}(T)}{\partial T}\dot{T} : \left([\mathbf{C}^{\mathrm{e}}(T)]^{-1} : \boldsymbol{\sigma}\right), \tag{15}$$

where the second term represents the contribution of the temperature dependence of the elastic constitutive tensor to the stress rate (Andrade-Campos et al., 2006; Kleiber, 1991; Ponthot and Papeleux, 2014). Accordingly, combining Eq. (13) and (15) the constitutive equation for the description of the thermoelastoplastic material behaviour in the current configuration is given by:

$$\dot{\boldsymbol{\sigma}}^{\mathrm{J}} = \mathbf{C}^{\mathrm{ep}} : \left(\mathbf{D} - \tilde{\mathbf{D}}^{\mathrm{th}}\right) + \dot{\boldsymbol{\sigma}}^{\mathrm{th}} \tag{16}$$

with,

$$\tilde{\mathbf{D}}^{\mathrm{th}} = \left(\frac{\partial [\mathbf{C}^{\mathrm{e}}(T)]^{-1}}{\partial T}\boldsymbol{\sigma} + \alpha_T^*(T)\mathbf{I}\right)\dot{T} \tag{17}$$

where $\mathbf{C}^{\mathrm{ep}}$ is the fourth-order tensor called elastoplastic modulus and $\dot{\boldsymbol{\sigma}}^{\mathrm{th}}$ represents the contribution of the temperature dependence of the work-hardening law. Both tensors, $\mathbf{C}^{\mathrm{ep}}$ and $\dot{\boldsymbol{\sigma}}^{\mathrm{th}}$, can assume different forms depending on the flow rule, work-hardening law and yield criterion adopted (Kleiber, 1991; Xing and Makinouchi, 2002a). Additionally, the computation of the elastoplastic modulus depends on the algorithm used for the integration of the constitutive model. Accordingly, it is possible to consider the tangent elastoplastic modulus or the consistent elastoplastic modulus. Regarding the algorithm used for the integration of the constitutive model currently adopted in DD3IMP, each increment is split into two phases. An explicit approach is used in the first phase, where the Euler's forward method is assumed for the integration of the constitutive model and hence the tangent elastoplastic modulus is used. The implicit approach is used in the second phase, where the Euler's backward method is adopted for the integration of the constitutive model. The consistent elastoplastic modulus is used to assure the quadratic convergence of the Newton–Raphson method. A detailed description of the derivation for both moduli can be found in (Alves, 2003; Barros et al., 2016; Oliveira et al., 2008).

2.1.2.1. Thermoplastic behaviour. In order to model the thermoplastic behaviour of the material, it is necessary to define the flow rule, the yield surface and its evolution. An associated flow rule is adopted, i.e. the plastic strain rate tensor is defined as

$$\mathbf{D}^{p} = \dot{\lambda}\frac{\partial \mathcal{F}(\bar{\sigma}, Y)}{\partial \boldsymbol{\sigma}}, \tag{18}$$

where $\dot{\lambda}$ is a scalar designated as the plastic multiplier, which can be determined by the consistency condition, i.e. $\dot{\mathcal{F}} = 0$. The scalar function $\mathcal{F}$ defines the yield surface and can be formulated as

$$\mathcal{F}(\bar{\sigma}, Y) = \bar{\sigma} - Y = 0, \tag{19}$$

where Y denotes the flow stress, while $\bar{\sigma}$ represents the equivalent stress. In this work, the von Mises yield criterion is adopted, accordingly $\bar{\sigma}$ is given by

$$\bar{\sigma} = \sqrt{\frac{3}{2}\boldsymbol{\sigma}' : \boldsymbol{\sigma}'} \tag{20}$$

where the $\boldsymbol{\sigma}'$ is the Cauchy deviatoric stress tensor.

For the yield stress evolution, a well-known hardening/softening law was selected, which has been adopted in several works (Armero and Simo, 1993; Canadija and Brnic, 2004; Ibrahimbegovic and Chorfi, 2002). This law is a combination of linear and saturation hardening, given by

$$Y(\bar{\varepsilon}^{\mathrm{p}}, T) = Y_0(T) + h(T)\bar{\varepsilon}^{\mathrm{p}} + [Y_\infty(T) - Y_0(T)][1 - \exp(-\delta\bar{\varepsilon}^{\mathrm{p}})], \tag{21}$$

where $\bar{\varepsilon}^{\mathrm{p}}$ is the equivalent plastic strain, while $h(T)$, $Y_\infty(T)$, $Y_0(T)$ and δ are the linear hardening modulus, the saturation stress, the initial yield stress and the hardening exponent, respectively. The thermal softening is included in this hardening law by defining some parameters as a function of the temperature, using the following relations

$$h(T) = h_0[1 - \omega_h(T - T_{\mathrm{ref}})] \tag{22}$$

$$Y_0(T) = Y_0[1 - \omega_0(T - T_{\mathrm{ref}})] \tag{23}$$

$$Y_\infty(T) = Y_\infty[1 - \omega_h(T - T_{\mathrm{ref}})] \tag{24}$$

where T_{ref} is the reference temperature and ω_0 and ω_h are the parameters for the description of the thermal softening. These relations can be improved in order to better describe the material behaviour (Ponthot and Papeleux, 2014).

2.1.3. Principle of virtual velocities

Consider that the body $\mathcal{B}$ is embedded in the spatial domain Ω at the time instant t and that Σ is its surrounding boundary. The boundary can be decomposed into two complementary parts ($\Sigma = \Sigma_v \cup \Sigma_\sigma$), i.e. Σ_v where the velocities are prescribed (Dirichlet's boundary condition) and Σ_σ where the Cauchy vector is prescribed (Neumann's boundary condition). Accordingly, assuming a *quasi*-static response and neglecting the body forces, the Cauchy's equilibrium equation and the boundary conditions for the body, in the local form, can be presented as

$$\begin{cases} \mathrm{div}(\boldsymbol{\sigma}) = 0 & \text{in } \Omega \\ \mathbf{t} = \bar{\mathbf{t}} = \boldsymbol{\sigma} n & \text{on } \Sigma_\sigma \\ \mathbf{v} = \bar{\mathbf{v}} & \text{on } \Sigma_v \end{cases}, \tag{25}$$

where $\mathbf{t}$ stands for the Cauchy stress vector (force per unit surface area in the current configuration), with $\mathbf{n}$ as the unit normal vector to the boundary Σ_σ, and $\mathbf{v}$ is the velocity vector. Thus, $\bar{\mathbf{t}}$ and $\bar{\mathbf{v}}$ are the prescribed values for the Cauchy stress vector and velocity, respectively.

In order to obtain the system of governing equations for the continuum body, the principle of virtual velocities is adopted. Hence, the deformable body $\mathcal{B}$ is in equilibrium if it verifies, for any $\delta\mathbf{v}$ virtual velocity field defined over the domain, the condition

$$\int_\Omega \boldsymbol{\sigma} : \delta\mathbf{D}\mathrm{d}\Omega = \int_{\Sigma_\sigma} \mathbf{t}^* \cdot \delta\mathbf{v}\mathrm{d}\Sigma_\sigma, \tag{26}$$

$\delta\mathbf{v}$ must verify the boundary condition of prescribed velocity, $\bar{\mathbf{v}}$ on Σ_v. This form of the principle of virtual velocities corresponds to the Eulerian description. In the framework of finite strains, it is necessary to adopt an updated Lagrangian formulation, to consider the large displacements and rotations. In this case, at each time interval, Eq. (26) needs to be rewritten regarding the last configuration that has been calculated. Therefore, within the time interval $[t,\ t+\Delta t]$, the last calculated configuration is C_0, corresponding to the time instant t. Thus, Eq. (26) assumes the following form

$$\int_{\Omega_0} \mathbf{S} : \delta\dot{\mathbf{F}}\mathrm{d}\Omega_0 = \int_{\Sigma_{0|\sigma}} \bar{\mathbf{t}} \cdot \delta\mathbf{v}\mathrm{d}\Sigma_{0|\sigma}, \tag{27}$$

where Ω_0 and Σ_0 are the domain and respective boundary occupied in C_0, at the time instant t. $\mathbf{S}$ is the first Piola-Kirchhoff stress tensor and $\bar{\mathbf{t}}$ is the prescribed Cauchy stress vector.

Regarding the time and spatial integration, the weak formulation of the equilibrium balance, Eq. (27), is linearized with respect to the incremental displacements for the implicit phase. In addition, it is also developed a tangent formulation for the explicit phase. Afterwards, the spatial discretization is carried out. A detailed description of these steps can be found in (Alves, 2003; Menezes and Teodosiu, 2000; Oliveira et al., 2008)

2.2. Thermal model

The numerical modelling of thermal and thermomechanical effects within a solid body requires the resolution of a transient heat transfer problem. In this section, the adopted formulation is described, as well as the time integration methods. It is based on the first principle of thermodynamics combined with the Fourier's law.

2.2.1. Heat conduction equation

Within a solid medium, such as body $\mathcal{B}$, the heat transfer can occur across the medium due to an existing temperature gradient. In thermomechanical problems, this temperature gradient within the solid body can be caused by several factors, such as heat generated by plastic deformation and frictional contact, heat losses for the environment (radiation and convection), among others. The differential equation governing the heat transfer within a solid medium, defined by the spatial domain Ω at the current configuration, can be derived from the first principle of thermodynamics (conservation of energy). Combined with the Fourier's law for heat conduction it assumes the following form:

$$\rho c \frac{\partial T}{\partial t} = \mathrm{div}[\mathbf{k} \cdot grad(T)] + \dot{w}^{\mathrm{p}} + \dot{q}, \quad \text{in } \Omega \ , \tag{28}$$

where ρ stands for the specific mass, c is the specific heat and $\mathbf{k}$ is the conductivity tensor. The thermal effect associated with the plastic deformation is taken into account by the coupling term $\dot{w}^{\mathrm{p}}$ and $\dot{q}$ corresponds to a heat source. The last term does not play any role in this work, thus it is neglected in the following analysis.

The internal heat generation by plastic deformation is the main heat driving source resulting from the mechanical problem. In Eq. (28), the term $\dot{w}^{\mathrm{p}}$ is used to model this phenomenon. This term corresponds to the fraction of the plastic power that is converted into heat, which is commonly expressed as

$$\dot{w}^{\mathrm{p}} = \chi\boldsymbol{\sigma} : \mathbf{D}^{\mathrm{p}}, \tag{29}$$

where χ is called the Taylor–Quinney factor, since it dates back to the experimental work of Taylor and Quinney (Taylor and Quinney, 1934). This factor is usually assumed to be a constant material parameter, ranging between 0.8 and 0.95 for metals. Since only a part of the plastic power dissipates as heat, the remaining part $(1-\chi)$ is assumed to be stored as energy in the material due to creation and rearrangement of microscopic defects and development of dislocations structures (Bever et al., 1973; Fekete and Szekeres, 2015; Ristinmaa et al., 2007). In contrast, the thermoelastic effect is not considered in the present study because it implies a temperature change around 0.2 K in metals, which is meaningless when compared with the effect of the heat generated by plastic deformation (Bever et al., 1973; Canadija and Brnic, 2004; Wriggers et al., 1992).

2.2.2. Principle of virtual temperatures and time integration

In order to solve Eq. (28), it is necessary to define an initial condition for the configuration at the instant $t=t_0=0$ and the boundary conditions on the surface Σ of the body. The initial condition corresponds to a temperature field

$$T(\mathbf{x}_0, t_0) = T_0(\mathbf{x}_0), \quad \text{in } \Omega_0, \tag{30}$$

where $T_0(\mathbf{x}_0)$ is the initial temperature defined for the body. The classical boundary conditions are the Dirichlet's boundary condition, which corresponds to an imposed temperature, and Neuman's boundary condition, which corresponds to an imposed heat flux. These conditions can be presented in the following form

$$\begin{cases} T = \bar{T}, & \text{on } \Sigma_T \\ q = -\mathbf{k}\cdot\text{grad}(T)\cdot\mathbf{n} = \bar{q}, & \text{on } \Sigma_q \end{cases}, \tag{31}$$

where the temperature $\bar{T}$ and the heat flux $\bar{q}$ are the prescribed values, which may vary with time. $\mathbf{n}$ stands for the unit normal vector to the boundary Σ_q. Thermal boundary conditions, such as convection, radiation and heat conduction by thermal contact, are important aspects to be considered in numerical models of thermomechanical problems (Bathe et al., 2000; Martins et al., 2016a;2016b). However, these are not addressed in this work, since they can be neglected to perform the comparison of the presented staggered algorithms, allowing to simplify the analysis.

In the same way as in the mechanical problem, the weak formulation was derived in order to obtain a suitable form to apply the finite element method. Thus, the principle of virtual temperatures is applied to Eq. (28) to express the heat flow equilibrium as

$$\int_\Omega \delta T \rho c \frac{\partial T}{\partial t} \mathrm{d}\Omega + \int_\Omega \text{grad}(\delta T)\cdot(\mathbf{k}\cdot grad(T))\mathrm{d}\Omega = \int_\Omega \delta T \dot{w}^{\mathrm{p}} \mathrm{d}\Omega + \int_{\Sigma_q} \delta T \bar{q} \mathrm{d}\Sigma_q. \tag{32}$$

The solution of Eq. (32), through the finite element method entails first the discretization of the whole spatial domain and, subsequently, the integration in time. Thus, the continuum body is discretized into finite elements, in which the temperature field and its time derivative are interpolated thanks to shape functions (Andrade-Campos et al., 2007; Martins et al., 2016a). The discretized finite element equations for heat transfer problems can be written in the matrix form as follows:

$$\mathbf{C}\dot{\mathbf{T}} + \mathbf{K}\mathbf{T} = \mathbf{Q}. \tag{33}$$

where $\mathbf{C}$ is the capacity matrix, $\mathbf{K}$ is the conductivity matrix and $\mathbf{Q}$ is the vector of nodal heat flux input. Accordingly, the solution of the transient heat conduction problem is reduced to the resolution of the set of ordinary differential equations (Eq. (33)). The α-method of time integration was chosen for the solution of this set of equations, which requires the use of the following equations (Andrade-Campos et al., 2007; Bathe, 1996):

$$\dot{\mathbf{T}}_{t+\Delta t} = \frac{\mathbf{T}_{t+\Delta t} - \mathbf{T}_t}{\Delta t}, \tag{34}$$

$$\mathbf{T}_{t+\alpha\Delta t} = (1-\alpha)\mathbf{T}_t + \alpha\mathbf{T}_{t+\Delta t}, \tag{35}$$

where t is the time instant and Δt the time increment. The parameter α can vary between 0 and 1. Depending on the value attributed to this parameter, the α-method takes the form of different integration methods, namely Euler's forward method ($\alpha=0$), Crank–Nicolson method ($\alpha=1/2$), Galerkin's method ($\alpha=2/3$) and Euler's backward method ($\alpha=1$).

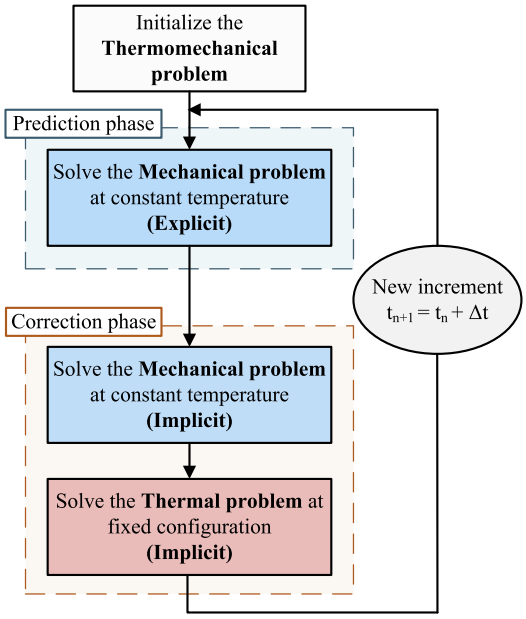

Fig. 1. Explicit algorithm for thermomechanical coupling.

3. Thermomechanical coupling

This section contains the main features of the classical staggered approaches adopted in the thermomechanical coupling, considering the isothermal split methodology, i.e. to solve the mechanical and the thermal problems sequentially. A new coupling algorithm is presented, which was developed considering the advantages and drawbacks of the classical approaches. In order to compare the proposed algorithm with the classical ones, all of them were implemented in the in-house finite element code DD3IMP.

3.1. Classical algorithms

As mentioned in Section 2, the evolution of the mechanical problem is described by a *quasi*-static formulation along with the transient heat transfer problem. The global thermomechanical problem is solved with the exchange of data between the two problems. Thus, the solution of the mechanical problem is a displacement field $\mathbf{u}$ determined for a constant temperature field $\mathbf{T}$. On the other hand, the solution of the thermal problem is a temperature field $\mathbf{T}$ for a fixed configuration, which corresponds to the result of a given displacement field $\mathbf{u}$. In order to solve the global thermomechanical problem, heat generation by plastic deformation, thermal softening and thermal strains are some of the effects that need to be taken into account for an accurate solution. Consequently, an efficient strategy for the data exchange between the two problems (mechanical and thermal) is required.

Within the staggered approach, two main coupling strategies exist for the treatment of the partitioned thermomechanical problem, the explicit strategy or single staggered and the implicit strategy or iterative strategy (Erbts and Düster, 2012; Matthies et al., 2006; Vaz et al., 2011). The explicit strategy presents the more straightforward implementation. In this case, the interchange of information between the two problems is performed only once, at each time increment. Fig. 1 illustrates schematically the explicit coupling algorithm, adapted to the structure of DD3IMP code. The first step is to solve the mechanical problem for a fixed temperature field, obtained in the previous time increment, allowing to obtain a trial displacement field. Since this trial displacement field does not satisfy the mechanical equilibrium equation, it is corrected based on an implicit approach with the Newton-Rapson

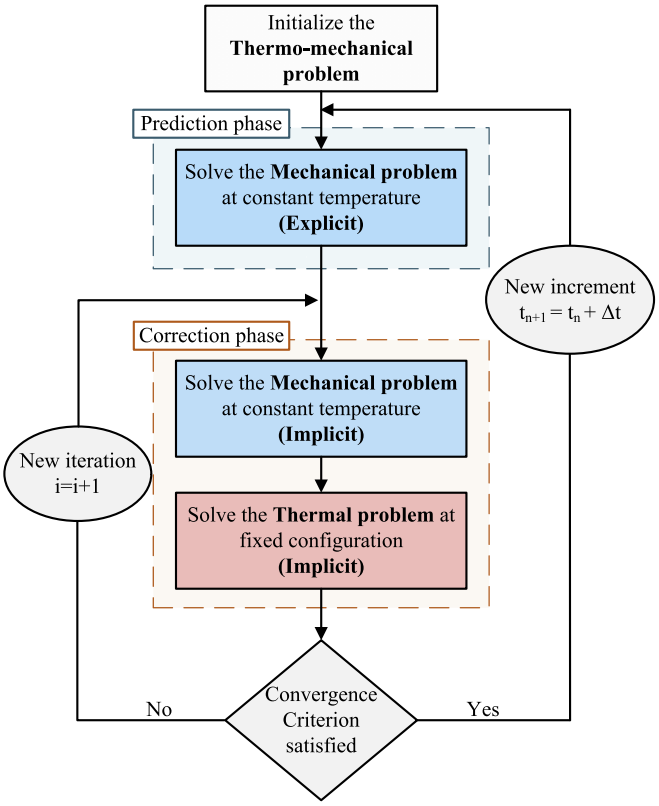

Fig. 2. Implicit algorithm for thermomechanical coupling.

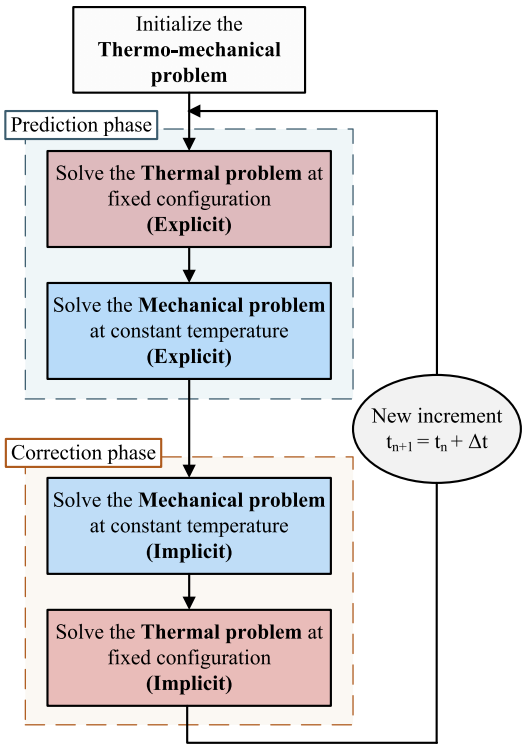

Fig. 3. Proposed algorithm for thermomechanical coupling.

method. The thermal problem is solved using this mechanical solution. Since the solution of the displacement field is always determined using the temperature field of the previous increment, a delay arises between the displacement field and the temperature field of the current increment, which induces a loss of accuracy. This problem can be circumvented at the expense of selecting a small time-step. Regardless the accuracy problem, the computational cost of the explicit strategy is relatively small due to the single sequential algorithm. An example of the application of this algorithm can be seen in the studies performed by Lee et al. (Lee et al., 2015; Vaz et al., 2011).

Another strategy commonly used in the treatment of the partitioned thermomechanical problems is denoted as implicit strategy or iterative strategy. This strategy attempts to achieve an accuracy similar to the one obtained with the monolithic approach. In this case, the interchange of information between the two fields is performed through an iterative procedure, aiming to reach the fully converged solution (Vaz et al., 2011). Fig. 2 illustrates the implicit algorithm adapted to the structure of DD3IMP code. The implicit algorithm is similar to the explicit one, except that the thermomechanical convergence criterion has to be fulfilled at each time increment (requiring an iterative cycle). The convergence criterion can be based on the dissipative energy, as used in the study of Dunić et al. (2016) or based on the body configuration as Erbts and Düster (2012). In the present study, the temperature field was chosen as criterion, i.e. convergence was assumed when the maximum difference between the temperature field of the last iteration and the current one is less than the defined tolerance (δ_{crit}), which can be expressed as

$$\max_n \left[\left(\left| T^{i+1}_{t+\Delta t} - T^{i}_{t+\Delta t} \right| \right)_n \right] < \delta_{\text{crit}} \text{ with } n = 1, .., NN, \tag{36}$$

where NN is the total number of nodes and i denotes the preceding iteration, whereas $i+1$ denotes the current iteration. Thus, whatever the coupling degree considered (strong or weak) at least two iterations are required in each increment to enable the evaluation of the convergence criterion (Erbts and Düster, 2012). This algorithm typically involves a higher computational cost due to the iterative cycle within each increment.

3.2. Proposed algorithm

The proposed coupling algorithm was developed to reach a better equilibrium between computational cost and accuracy of results. The main difference to the classical staggered algorithms is the way that the information between the problem fields is interchanged. Within each increment, the proposed algorithm is divided into two phases, a prediction phase and a correction phase, as shown in Fig. 3. In both phases, the thermal and the mechanical problem are solved using different numerical methods and considering distinct input data. The prediction phase aims to give a trial solution for the problem, which is not accurate, but assures an improvement of the convergence rate during the iterative procedure in the single field problems, performed using an implicit approach.

The prediction phase begins with the resolution of the thermal problem, which is solved for a user-defined time-step, adopting an explicit or semi-implicit approach (depending on the value defined for the parameter α in Eq. (35)). Since the solution of the displacement field is unknown at the moment and, consequently, the fraction of plastic power converted into heat ($\dot{w}^{\text{p}}$, in Eq. (28)), which plays an important role in the temperature evolution, is also unknown. Therefore, in order to minimize the error resulting from neglecting this term, the trial temperature field is evaluated assuming that fraction of plastic power converted into heat in the current increment is the same as in the previous increment. Based on this, the amount of energy generated by plastic deformation is estimated for every integration point, allowing to determine a trial temperature field. After that, the mechanical problem is solved considering the trial temperature field obtained previously and adopting an explicit method. The solution sequence in the prediction phase is a key point because the material properties

used in the mechanical solution (based on an explicit approach) are updated according to the trial temperature field, which is expected to lead to an improved solution.

At the end of the prediction phase, a trial displacement field and a trial temperature field are available. However, neither the trial temperature field nor the displacement satisfies the equilibrium equations. Therefore, these trial solutions are corrected using an implicit method for the time integration of the respective equations of equilibrium. For the non-linear system of equations resulting from the thermoelastoplastic problem, with large deformations, an iterative method of Newton–Raphson type is adopted. The global convergence rate of the Newton–Raphson method can be improved with a good estimative of the initial solution, highlighting the importance of the prediction phase. During the correction phase the mechanical problem is solved first (see Fig. 3), using the trial temperature field. Thus, the previous displacement field, which corresponds to the initial solution for the Newton-Raphson method, is corrected until the equilibrium state is attained. Finally, the thermal problem is solved using an implicit approach (with the parameter $\alpha = 1$ in Eq. (35)) for the current equilibrium configuration.

4. Numerical examples

This section contains three different numerical examples, carefully selected to validate the developed finite element code in the resolution of thermomechanical problems and compare it with the aforementioned classical coupling strategies.

In the three numerical examples, 8-node trilinear solid elements were chosen for the spatial discretization of the deformable body. For the mechanical problem, a selective reduced integration technique (Hughes, 1980) is adopted to avoid volumetric locking in elastoplastic problems (Menezes and Teodosiu, 2000). For the resolution of the thermal problem, full integration was adopted (Adam and Ponthot, 2005). Also regarding the thermal problem, the prediction phase is performed with the Crank-Nicolson method ($\alpha = 1/2$ in Eq. (35)) while the Euler's backward method ($\alpha = 1$ in Eq. (35)) is used for the correction phase, in order to avoid stability problems (Bathe, 1996). The value adopted for the convergence criterion for the implicit algorithm, defined in Eq. (36), was $\delta_{\text{crit}} = 0.01$K. Note that tests performed with a value of $\delta_{\text{crit}} = 1 \times 10^{-5}$K lead to a negligible difference in the results.

As previously mentioned, the thermomechanical algorithms were implemented in the FE solver DD3IMP, which resorts to an automatic time-step control technique to restrict the increment size, called $r_{\min}$ strategy (Oliveira and Menezes, 2004; Yamada et al., 1968). This strategy analyses the evolution of state variables and boundary conditions between the last converged configuration and the one obtained in the prediction stage, using the increment size predefined by the user (trial configuration). Based on maximum variation criteria the coefficient $r_{\min} \in [0; 1]$ is determined, such that if $r_{\min} \neq 1$ the trial configuration must be corrected to obtain the initial solution for the correction stage. Previous results indicate that for contact problems, the first increment of the process presents convergence problems. Therefore, an additional feature of the $r_{\min}$ strategy implemented for the mechanical problem is that the size of the first increment is always much smaller (at least $10\times$) than the value predefined by the user (Alves, 2003). This feature of the $r_{\min}$ strategy is maintained in all examples analysed, even when a constant time-step is used. The three examples are solved with a constant time-step and the last one is also solved activating the $r_{\min}$ strategy, in order to assess the performance of three coupling algorithms in both conditions.

All numerical simulations presented were performed on a computer machine equipped with an Intel® Core i7–4720HQ Quad-Core processor (2.6 GHz) and the Windows® 10 (64-bit platform) operating system.

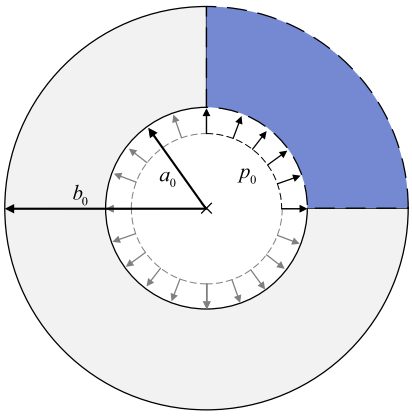

Fig. 4. Expansion of an infinite thick-walled cylinder (inner radius $a_0 = 100$ mm and outer radius $b_0 = 200$ mm) subject to an internal pressure (p_0).

4.1. Thermoplastic cylinder under internal pressure

The purpose of this benchmark, used by several authors (Adam and Ponthot, 2005; Andrade-Campos et al., 2007; Ibrahimbegovic and Chorfi, 2002), is to assess the robustness and accuracy of the developed finite element code. This example deals with the radial expansion of a thick-walled infinite cylinder, caused by an internal pressure applied on the inner surface. Accordingly, the deformation process is accompanied by a temperature growing, resulting from the heat generated by plastic deformation. This example was firstly proposed by Argyris and Doltsinis (Argyris and Doltsinis, 1981) as a non-isothermal problem and later adapted by Simo and Miehe (Simo and Miehe, 1992).

The thick-walled cylinder is schematically depicted in Fig. 4, which is assumed infinite along the axial direction, allowing to use plane strain conditions. Due to the symmetry conditions, only one-fourth of the cylinder was modelled, using 10 finite elements along the hoop direction and 10 finite elements through the thickness direction. Following the study of Simo and Miehe (Simo and Miehe, 1992), the internal pressure was replaced by a prescribed radial displacement $\bar{u} = 130$mm on the inner surface, which is applied for a constant velocity $\dot{u} = 1$mm/s. Therefore, the internal pressure required to ensure this prescribed displacement is the variable under analysis. Regarding the boundary conditions for the thermal problem, the cylinder is assumed thermally isolated and the initial temperature is 293 K. Thus, the problem is driven by thermal initial condition and the prescribed radial displacement, leading to large plastic deformation of the cylinder accompanied by heating. The material parameters adopted by Simo and Miehe (Simo and Miehe, 1992) are recalled in Table 1, which define the linear strain hardening (in this example, the saturation hardening is not considered, i.e. $\delta = 0$ in Eq. (21)) and the thermal softening.

A constant time-step of $\Delta t = 6.5$s was chosen, except the first and the last increments. The first step, as mentioned early, is smaller $\Delta t_{\text{initial}} = 0.1 \times \Delta t$ and the last one is adjusted to achieve the prescribed total time ($t = 130$ s). Thus, the loading is carried out in 21 time-steps. Despite the very large deformation in the cylinder, it is possible to obtain a converged solution with only a few time-steps, as previously reported by Simo and Miehe (Simo and Miehe, 1992). The selection of 21 increments is based on the fact that the same authors also reported that, for the adiabatic split, the temperature evolution obtained via a Crank-Nicolson temperature-integrator yields nearly exact results for a number of time-steps higher than 20.

Table 1
Material parameters for the thermoplastic cylinder under internal pressure.

Young's modulus	E	70,000 MPa
Poisson's ratio	ν	0.3
Initial yield stress	Y_0	70 MPa
Linear hardening modulus	h_0	210 MPa
Thermal softening	ω_0	$3.0\times10^{-4}\mathrm{K}^{-1}$
Hardening softening	ω_h	$0.0\ \mathrm{K}^{-1}$
Hardening exponent	δ	0.0
Thermal expansion coef.	α_T	$23.8\times10^{-6}\mathrm{K}^{-1}$
Specific mass	ρ	$2900\mathrm{kgm}^{-3}$
Specific heat	c	$900\mathrm{Jkg}^{-1}\mathrm{K}^{-1}$
Conductivity	k	$150\mathrm{Wm}^{-1}\mathrm{K}^{-1}$
Taylor-Quinney factor	χ	0.9
Reference temperature	T_ref	293 K

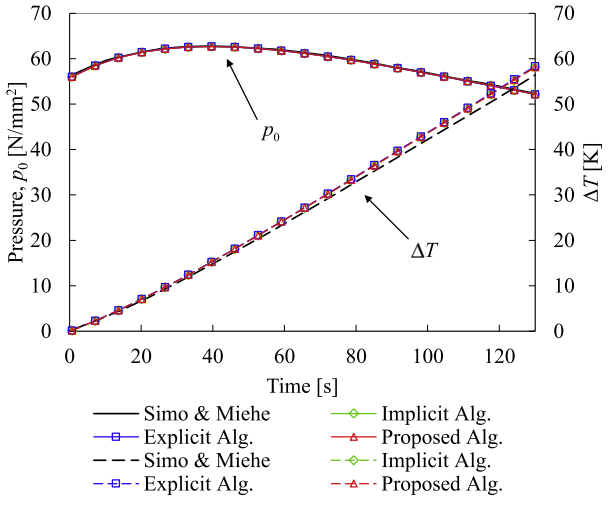

Fig. 5. Evolution of the internal pressure and relative temperature ($\Delta T = T_\mathrm{i} - T_\mathrm{ref}$) at the inner surface of the cylinder, considering the adiabatic case.

Fig. 5 presents the evolution of the internal pressure and the relative temperature of the inner surface of the cylinder considering the adiabatic process, i.e. the internal heat conduction is not considered, comparing the three coupling algorithms (explicit, implicit and proposed) with the results from Simo and Miehe (Simo and Miehe, 1992). The results show that the pressure increases slightly after the cylinder attains plastic deformation and then decreases smoothly, due to the thermal softening. On the other hand, the relative temperature ($\Delta T = T_\mathrm{i} - T_\mathrm{ref}$) increases approximately linearly, as shown in Fig. 5. The three algorithms show very good agreement with the numerical results obtained by Simo and Miehe (Simo and Miehe, 1992), for the internal pressure. However, for the temperature evolution, the results are slightly overestimated by the three algorithms. Indeed, the combination of a staggered scheme with the Euler's backward method for the thermal problem tends to overestimate the temperature (see e.g. (Adam and Ponthot, 2005; Simo and Miehe, 1992)).

The deformed configuration of the cylinder with the relative temperature distribution at instants $t = 26.65$, 85.15 and 130 s is presented in Fig. 6. Due to the difference in the expansion of the inner and outer cylinder radius, the thickness decreases during the loading. The maximum value of relative temperature occurs in the inner surface since the plastic strain is higher in this region.

In order to analyse the influence of the internal heat conduction on the final temperature distribution, different loading times are considered. The temperature distribution along the radial direction at the end of the process is presented in Fig. 7 for different durations of the test, such as $t = 1.3$, 13, 130 s and the adiabatic case. Since the heat source (plastic deformation) is stronger in the inner surface of the cylinder, the temperature is always higher in the inner surface than in the outer surface, particularly for the fast loading cases. Due to the effect of heat conduction, the thermal gradient within the cylinder thickness decreases with the increase of the process time duration, as shown in Fig. 7. For the limit case $t \to \infty$ the attained temperature is homogeneous through the cylinder thickness (relative temperature of approximately 31 K).

Table 2
Computational performance of the different coupling algorithms used in the thermoplastic cylinder under internal pressure example (adiabatic case).

	Implicit Alg.	Explicit Alg.	Proposed Alg.
Nº increments	21	21	21
CPU time [s]	25	21	22

Table 3
Material parameters used in the elementary uniaxial tensile test.

Young's modulus	E	206,900 MPa
Poisson's ratio	ν	0.29
Initial yield stress	Y_0	450 MPa
Saturation stress	Y_∞	715 MPa
Linear hardening modulus	h_0	129.24 MPa
Thermal softening	ω_0	$2.0\times10^{-3}\mathrm{K}^{-1}$
Hardening softening	ω_h	$2.0\times10^{-3}\mathrm{K}^{-1}$
Hardening Exponent	δ	16.93
Thermal expansion coef.	α_T	$1.0\times10^{-5}\mathrm{K}^{-1}$
Specific mass	ρ	$7800\mathrm{kgm}^{-3}$
Specific heat	c	$460\mathrm{Jkg}^{-1}\mathrm{K}^{-1}$
Conductivity	k	$45\mathrm{Wm}^{-1}\mathrm{K}^{-1}$
Taylor–Quinney factor	χ	0.9
Reference temperature	T_ref	293 K

Table 2 presents the CPU time required by each coupling algorithm to carry out the thermomechanical simulation, considering the adiabatic case (see Fig. 5). Since this example is a small dimension benchmark problem (solved using 21 increments), the difference in computational cost between the three algorithms is negligible. Nonetheless, it should be mentioned that the implicit algorithm is the one requiring the highest CPU time, whereas the explicit and the proposed algorithm require almost the same CPU time.

4.2. Elementary uniaxial tensile test

The main objective of this example is to analyse the influence of the (constant) time-step in the accuracy of the proposed coupling algorithm and compare it with the classical algorithms described in Section 3.1. This example involves a single finite element (linear hexahedral) submitted to an uniaxial tensile stress, imposed by a prescribed displacement on a face $\bar{u} = 2$ mm, at constant velocity $\dot{u} = 1$mm/s. The initial configuration of the finite element ($1\times1\times1$ mm^3) is schematically represented in Fig. 8, including the adopted boundary conditions and the prescribed nodal displacements. The finite element is considered thermally isolated from the environment and the heat generated by plastic deformation is the only heat source. The initial temperature was defined as 293 K. The material parameters used in this example are listed in Table 3.

Since the time-step size is a key factor in the thermomechanical coupling when staggered approaches are adopted, two different sizes have been chosen to perform this analysis, namely a constant time-step of $\Delta t = 0.2$ s (10 increments) and a constant time-step of $\Delta t = 0.04$ s (50 increments). In both cases, the first step is carried out with a significantly smaller time-step size $\Delta t_\mathrm{initial} = \Delta t \times 0.1$s. Due to the uniform elongation imposed on the finite element and the fact that there are no heat fluxes, the value of all state variables

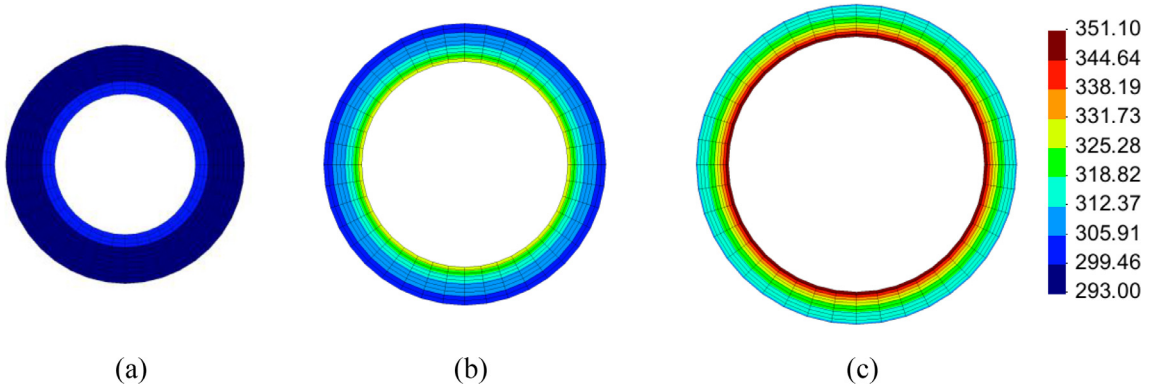

Fig. 6. Deformed configuration of the thermoplastic cylinder at different instants and contour plot of temperature (adiabatic case): (a) $t=26.65$ s (b) $t=85.15$ s and (c) $t=130$ s.

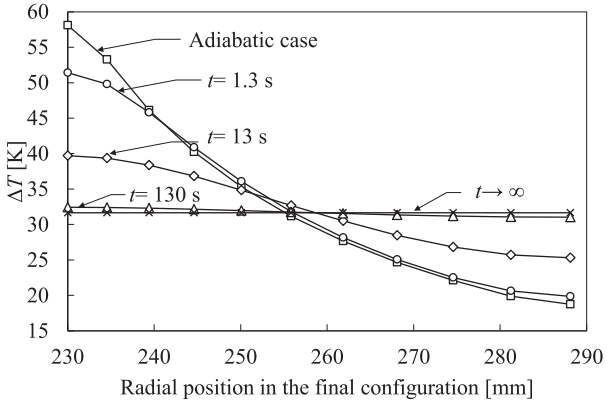

Fig. 7. Distribution of the relative temperature ($\Delta T=T_i-T_{ref}$) along the radial direction for the final configuration, considering different values for the loading duration (obtained with the proposed algorithm).

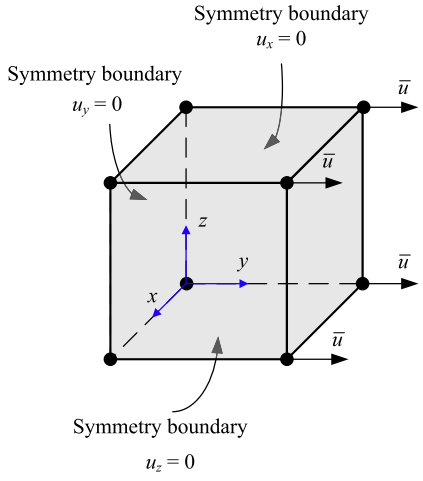

Fig. 8. Initial configuration of the hexahedral finite element with boundary conditions and prescribed nodal displacements.

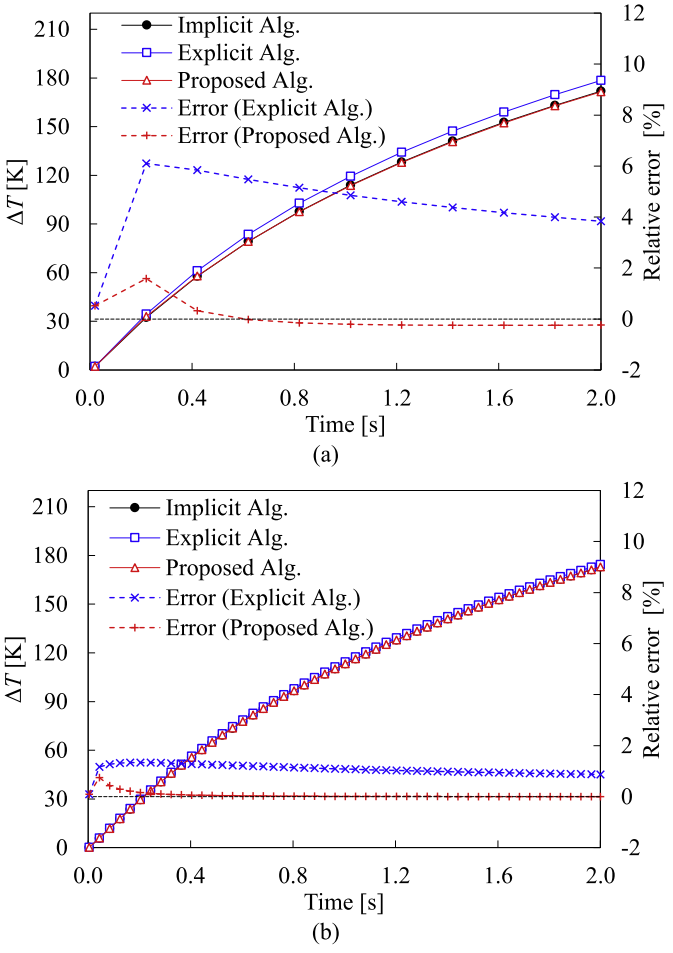

Fig. 9. Evolution of the relative temperature ($\Delta T=T-T_0$) obtained with the different coupling algorithms and relative error considering the implicit coupling strategy as reference: (a) time-step $\Delta t=0.2$ s and (b) time-step $\Delta t=0.04$ s.

(stress, strain and temperature) is uniform within the element during the entire loading.

The evolution of the relative temperature predicted by each coupling algorithm is presented in Fig. 9, comparing the two time-step sizes. The temperature increases gradually due to the heat generated by plastic deformation. However, the temperature rate decreases during the loading, since the prescribed displacement is applied at constant velocity but the length of the finite element is increasing in this direction, leading to a decreasing plastic strain rate. For both step sizes, the solution provided by the proposed coupling algorithm is closer to the one obtained with the implicit coupling strategy, as highlighted in Fig. 9. In order to quantify the difference between the coupling algorithms, the relative error is evaluated considering the implicit coupling strategy as the reference. It can be assumed that it presents superior accuracy due to the iterative cycle within each time increment. The relative error is

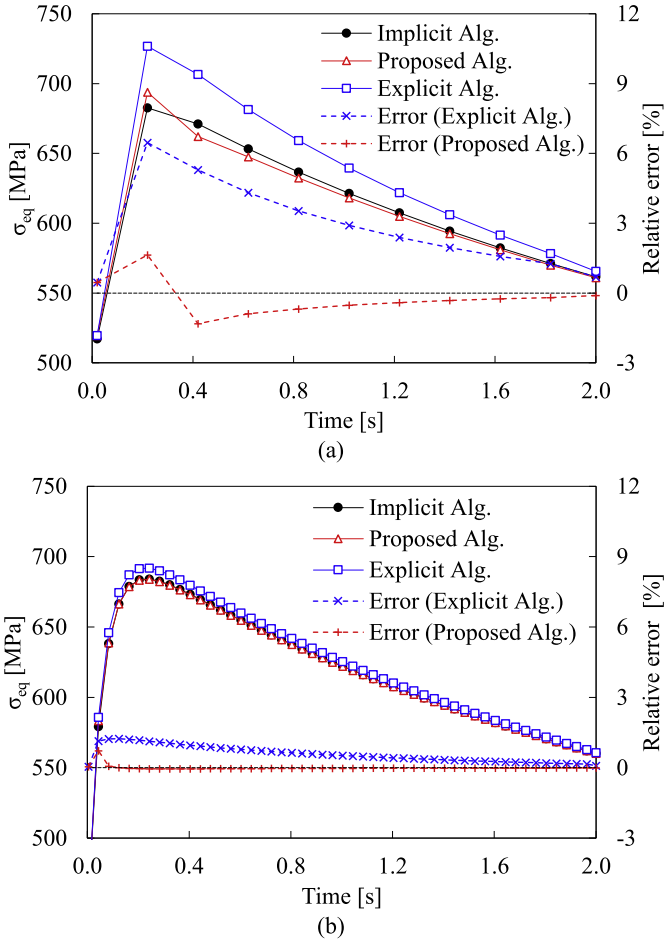

Fig. 10. Evolution of the equivalent von Mises stress obtained with the different coupling algorithms and relative error considering the implicit coupling strategy as reference: (a) time-step $\Delta t = 0.2$ s and (b) time-step $\Delta t = 0.04$ s.

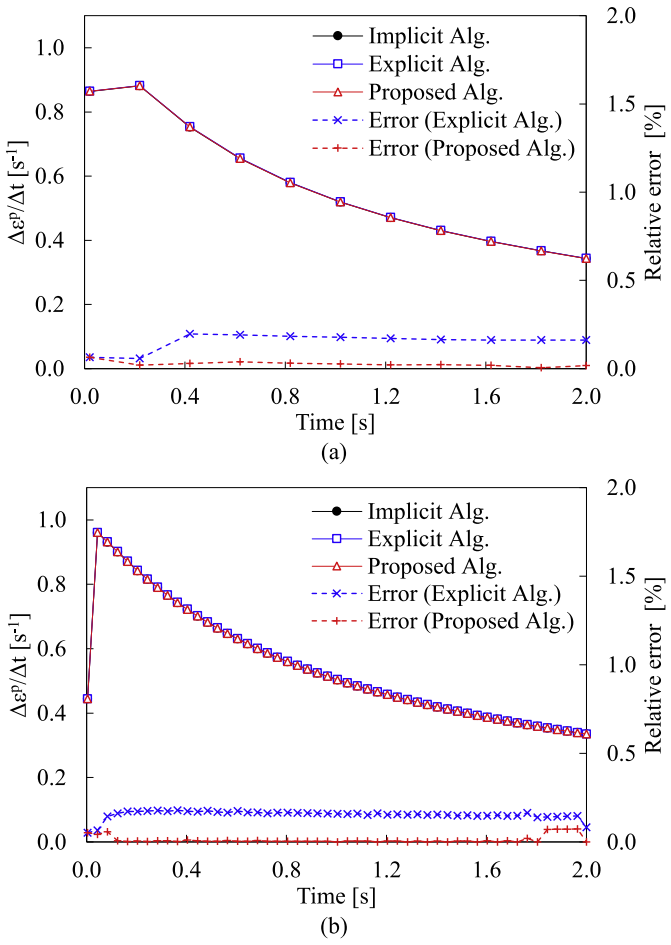

Fig. 11. Evolution of the plastic strain rate obtained with the different coupling algorithms and relative error considering the implicit coupling strategy as reference: (a) time-step $\Delta t = 0.2$ s and (b) time-step $\Delta t = 0.04$ s.

defined as

$$\text{Relative error} = \frac{T - T^{\text{implicit}}}{T^{\text{implicit}}} \times 100\ [\%], \tag{37}$$

where T and T^{implicit} are the temperature values calculated with the algorithm under analysis and with the implicit algorithm, respectively. Note that the same definition is used for the other variables under analysed. The relative error of both the proposed and the explicit coupling algorithms is presented in Fig. 9. The relative temperature is overestimated (positive error value) by the explicit algorithm and globally underestimated (negative error value) by the proposed algorithm. Despite the decrease of the relative error with the reduction of the increment size, the error of the predicted temperature is always significantly lower considering the proposed algorithm (see Fig. 9). In fact, the explicit coupling algorithm provides a temperature evolution with a relative error ranging between 1 and 1.5% using the small increment size (see Fig. 9 (b)), while the proposed algorithm gives a temperature solution with an error lower than 0.5% (except for the second increment) using the large increment size (see Fig. 9 (a)).

The evolution of the equivalent von Mises stress predicted by each coupling algorithm is shown in Fig. 10, comparing the two time-step sizes. The equivalent stress increases abruptly at the beginning and then decreases with a tendency approximately linear. The increase of temperature (see Fig. 9) activates the thermal softening mechanisms, which decreases the flow stress and consequently the equivalent stress, as shown in Fig. 10. The adoption of a smaller time increment leads to smaller differences between the coupling algorithms in terms of equivalent stress, as previously observed for the temperature evolution. For both step sizes studied, the equivalent stress is overestimated (positive relative error) by the explicit coupling algorithm and globally underestimated (negative relative error) by the proposed algorithm, as shown in Fig. 10. The positive relative error observed in the explicit coupling algorithm is related to the delay in the temperature field update (temperature of the previous increment), which consequently delays the softening mechanisms. Thus, the amount of heat generated by plastic deformation is overestimated (Fig. 9) due to the overestimation of the equivalent tensile stress. Besides, the magnitude of the equivalent stress error is decreasing because the temperature rate decreases during the loading (see Fig. 9). The relative error of the equivalent stress predicted by the proposed coupling algorithm is substantially lower, as shown in Fig. 10, being insignificant for the small increment size. The improvement in the results accuracy comes from the resolution of the mechanical problem using the trial temperature field of the current increment, which is calculated in the prediction phase (Fig. 3). As explained in Section 3.2, in the proposed algorithm, the prediction phase of the thermal problem is carried out considering that the fraction of plastic power converted into heat is the same of the previous increment, i.e. it is assumed that both the flow stress and the plastic strain rate from the previous increment will remain in the current increment. Therefore, the trial temperature is slightly overestimated because both the flow stress (see Fig. 10) and the plastic strain rate (see Fig. 11) present a decreasing evolution after a few

initial increments. Consequently, the equivalent stress (Fig. 10) is slightly underestimated in these increments due to the resolution of the mechanical problem using the overestimated trial temperature (see Fig. 3).

The plastic strain rate evolution predicted by each coupling algorithm is shown in Fig. 11, which also compares the two time-step sizes. Since the increment of plastic strain is mainly dictated by the prescribed nodal displacements, the difference between the coupling algorithms is negligible, as shown in Fig. 11. Indeed, the relative error is always lower than 0.2% for both step sizes analysed. The first increment is slightly off the trend, because its size is very small, thus leading to a substantial part of the deformation being elastic. When using the proposed algorithm, the heat generated by plastic deformation for the second increment is predicted based on the fraction of plastic power (see Eq. (29)) determined in the previous one. However, due to the automatic time-step control technique this first increment is mainly elastic. Thus, the value predicted for the fraction of plastic power in the prediction phase is underestimated for the second increment, leading to the underestimation of the trial temperature. However, since some fraction of plastic power is taken into account, when using the proposed algorithm, the solution presents a lower error.

For the explicit algorithm, since the mechanical problem is solved assuming the same temperature field as in the previous time-step, one can expect that the temperature would be overestimated (underestimated) when the plastic strain rate is decreasing (increasing). This holds for the example under analysis, which presents a decreasing plastic strain rate (see Fig. 11) with a consequent overestimation of the temperature (see Fig. 9). For the implicit algorithm, although the mechanical problem is solved in the first iteration assuming the same temperature field as in the previous time-step, the mechanical and thermal fields are iteratively updated until convergence is attained. This results in the attenuation of the delay imposed by the prediction stage in the temperature field. For the proposed algorithm, a trial temperature field is determined assuming that the fraction of plastic power converted into heat is the same as for the previous increment. Considering that after a few initial increments, both the plastic strain rate (see Fig. 11) and the equivalent von Mises stress (see Fig. 10) present a decreasing trend, this means that this assumption will lead to an overestimation of the trial temperature field. Consequently, the equivalent von Mises stress field, determined in the correction phase, will be underestimated. For this example, the plastic strain increment is mainly dictated by the imposed displacement, as explained before. Therefore, as shown in Fig. 11, the evolution predicted for the plastic strain rate is similar, whatever the algorithm adopted. Thus, the amount of heat generated by plastic strain will be underestimated in the correction phase of the thermal problem, as a consequence of the underestimation of the equivalent von Mises stress field. This results in the observed underestimation of the current temperature field (see Fig. 9).

4.3. Thermoplastic cylindrical bar

The purpose of this example is to compare the computational performance of the proposed coupling algorithm with the classical ones described in Section 3.1, considering both a constant and a variable time-step size. First, the cylindrical bar is submitted to simple tension using a constant time-step. Afterwards, the cylindrical bar is submitted to tension followed by compression considering a non-constant time-step size, which also allows to assess the performance of the proposed algorithm in case of loading-unloading.

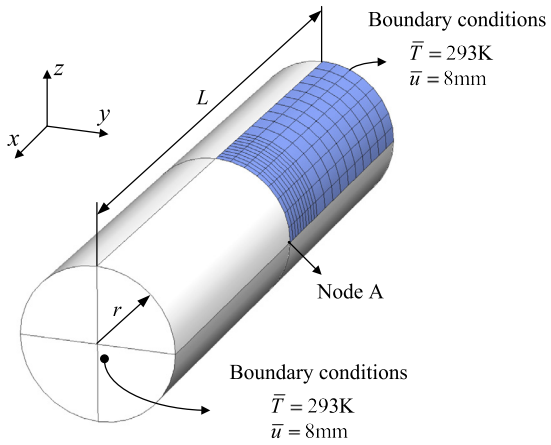

Fig. 12. Configuration of the cylindrical bar submitted to traction forces, including the finite element mesh of one-eighth.

4.3.1. Bar submitted to simple tension

This first case considers a cylindrical bar submitted to traction forces, which is self-heated due to the heat generated by plastic deformation. The cylindrical bar has no imperfections and presents a constant cross-section along the x-axis, defined by the radius r= 6.413mm, and a length L= 53.334mm. The traction forces are imposed at the two ends of the bar by means of a prescribed displacement $\bar{u} = 8$ mm, using a constant velocity of $\dot{u} = 1$mm/s. A constant time-step of $\Delta t = 0.24$ s was chosen for this example, except for the first and the last steps. The first step is carried out with a significantly smaller value $\Delta t_{\text{initial}} = \Delta t \times 0.1$s, as previously explained, while the last one is adjusted to fit the prescribed total time. Due to symmetry conditions, only one-eighth of the bar was modeled. The initial configuration of the cylindrical bar is presented in Fig. 12, as well as the finite element mesh for one-eighth of the bar. The adopted finite element mesh contains 960 solid linear finite elements (see Fig. 12). The thermomechanical material properties are identical to those adopted in the last example, which are presented in Table 3. The bar is thermally isolated and its initial temperature was defined as 293 K. The temperature is also prescribed at the two ends of the bar and is kept constant during the loading.

The stress state in the specimen is homogeneous at the beginning of the loading, although it changes due to the temperature gradient developed during the stretching of the bar. This gradient results from the heat generated by plastic deformation and the constant temperature prescribed on the two ends of the bar. The temperature distribution along the axial axis of the bar is presented in Fig. 13 for four different instants. The temperature gradient induces the occurrence of shear stress in the middle of the specimen and the necking phenomenon is triggered (Wriggers et al., 1992). The strain localization generates a severe local temperature increase and a consequent decrease of the flow stress due to thermal softening.

Fig. 14 and Fig. 15 present the equivalent von Mises stress and the equivalent plastic strain distributions, respectively, both plotted in the deformed configuration of the bar. These results were predicted with the proposed coupling algorithm. The strain localization in the middle of the specimen, resulting from the temperature gradient in the bar, is highlighted in Fig. 15. The stress distribution just after necking is presented in Fig. 14 (a). After that instant, the localization of the equivalent stress in the central area of the bar occurs, reducing considerably the value of the von Mises stress close to the extremities (see Fig. 14 (c)).

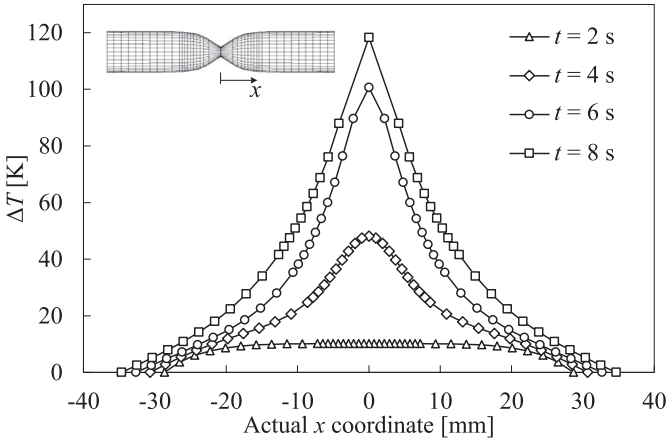

Fig. 13. Distribution of the relative temperature along the axial axis of the bar for four different instants (predicted with the proposed coupling algorithm).

The evolution of the force in the cylindrical bar is presented in Fig. 16, comparing the three different coupling algorithms. The force presents an increasing tendency until necking, after which it gradually decreases. The difference between the coupling algorithms is highlighted in the predicted force value after the onset of necking. In fact, the differences are negligible before this point. Additionally, it should be mentioned that the instant of maximum load predicted by the proposed algorithm is similar to the implicit algorithm, while the explicit algorithm presents a delay at this point. These results highlight that the onset of necking is very sensitive to the coupling strategy adopted. The relative error is also presented in Fig. 16. After necking, the force is overestimated (positive error value) by both the explicit and the proposed algorithms, as shown in Fig. 16. However, the force error is at least two times lower using the proposed algorithm than the explicit coupling algorithm.

The relative temperature evolution in node A (see Fig. 12) is presented in Fig. 17 for the three coupling algorithms. The temperature rate is significantly higher after necking, since the plastic zone is confined to the necked area in the middle of the bar, as illustrated in Fig. 15. Thus, a strong rise in temperature takes place in this area while the end of the bar remains at an approximately constant temperature. In addition, the temperature in node A becomes approximately constant at the end of loading, due to the necking localization in the middle of the bar and the constant temperature prescribed on the two ends. Such as in the force evolution, the relative error of the temperature is insignificant until the onset of necking (Fig. 17). After that, the error is negative (the temperature is underestimated), becoming slightly positive at the end.

The evolutions of the equivalent plastic strain rate and the flow stress are presented in Fig. 18, for the gauss integration point nearest to node A. The negative error in the temperature evolution is a consequence of the underestimation of the plastic strain rate (Fig. 18 (a)), which in turn is a consequence of the overestimation of the flow stress (Fig. 18 (b)). The error in the equivalent plastic strain rate results in a lower value of the fraction of plastic power converted into heat and, consequently, leads to a lower temperature value. These results are consistent with the ones previously reported for the elementary uniaxial tensile test (see Section 4.2), since in that case the plastic strain rate has a decreasing trend. In the cylindrical bar the plastic strain rate presents a constant value before the onset of necking, as a result of the heat fluxes. However, after the onset of necking (see Fig. 18 (a)), in the proposed algorithm, the increasing tendency of the plastic strain rate contributes to the underestimation of the trial temperature. Moreover, as expected, the temperature is underestimated for the explicit algorithm, since the plastic strain rate is increasing. The relative error of the flow stress, evaluated at point A, is different from the error observed for the force, since the last is a global variable and the stress field is not homogeneous.

Concerning the accuracy of the proposed algorithm, the value of the relative error in the temperature is at least two times lower using the proposed algorithm than the explicit coupling algorithm, as shown in Fig. 17. Indeed, the maximum magnitude of the error attained using the explicit algorithm is about 12% while for the proposed it is a value inferior to 6%.

The computational performance of the algorithms has been evaluated based on the CPU time required by each coupling algorithm, using 35 increments to carry the thermomechanical simulation. The CPU time for the different algorithms is presented in Table 4. The computational cost of the implicit coupling algorithm is substantially higher than the other two algorithms. In fact, the computational time required by the proposed algorithm is only slightly larger than the one required by the explicit coupling algorithm (see Table 4), which is about half the time required by the implicit coupling algorithm. The iterative cycle inherent to the implicit coupling algorithm requires the solution of both the mechan-

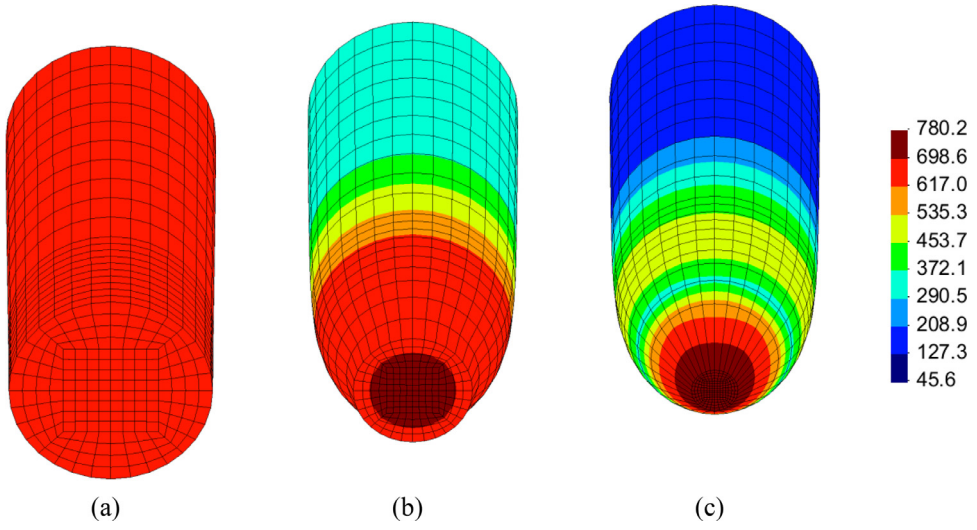

Fig. 14. Equivalent von Mises stress [MPa] distribution plotted in the deformed configuration of the cylindrical bar: (a) $t=3$ s, (b) $t=6$ s and (c) $t=8$ s.

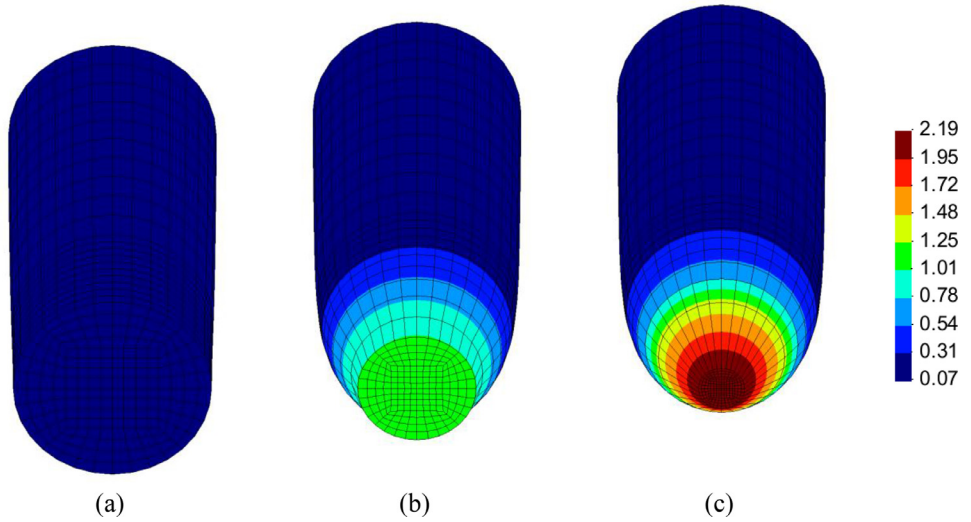

Fig. 15. Equivalent plastic strain distribution plotted in the deformed configuration of the cylindrical bar: (a) $t=3$ s, (b) $t=6$ s and (c) $t=8$ s.

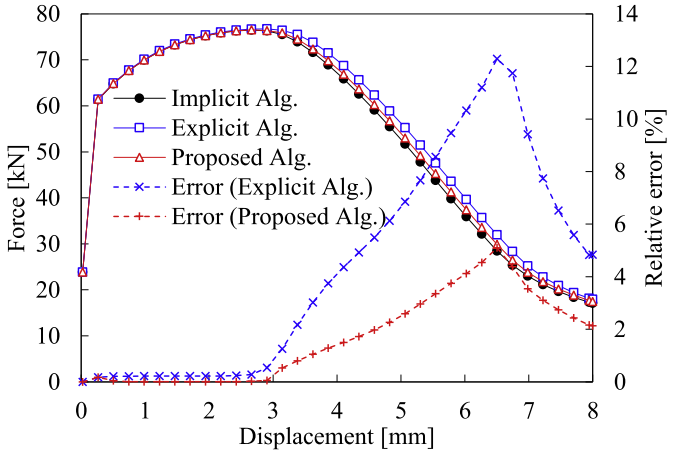

Fig. 16. Evolution of the force in the cylindrical bar obtained with different coupling algorithms and the relative error considering the implicit coupling strategy as a reference.

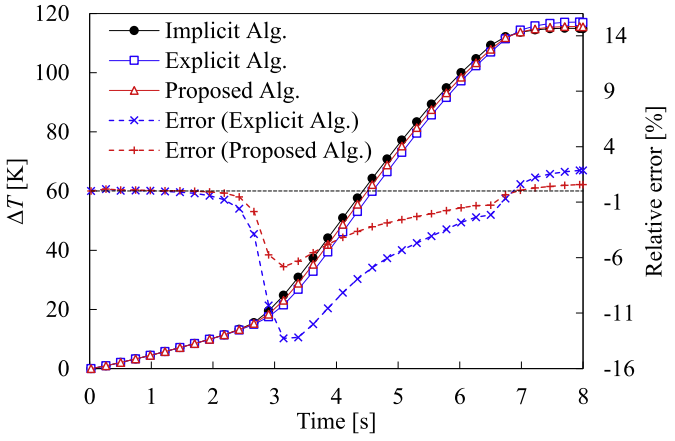

Fig. 17. Evolution of the relative temperature predicted in node A (see Fig. 12) using the different coupling algorithms and the relative error considering the implicit coupling strategy as a reference.

Table 4
Computational performance of the different coupling algorithms used in the cylindrical bar submitted to simple tension example.

	Implicit Alg.	Explicit Alg.	Proposed Alg.
Nº increments	35	35	35
CPU time [s]	289	113	114

ical and the thermal problems in the correction phase, until the convergence criterion is attained. Moreover, although the thermal problem is also solved in the prediction phase of the proposed algorithm, since an explicit approach is adopted, the increase in the computational time observed when comparing with the explicit coupling algorithm is not significant. Therefore, the proposed coupling algorithm provides numerical solutions for thermomechanical problems with computational cost identical to the explicit algorithm, although with significantly better accuracy.

4.3.2. Bar submitted to reverse loading

In the second loading case, the bar (same geometry and finite element mesh, previously presented in Fig. 12) is subjected to tension followed by compression. Hence, during the first stage, traction forces are imposed at the two ends of the bar by means of a prescribed displacement $\bar{u} = 5$ mm. In the second stage, the loading path is inverted and compression forces are imposed at the two ends of the bar, by means of a prescribed displacement $\bar{u} = -5$mm. The loading velocity is assumed constant during the entire test ($\dot{u} = 1$ mm/s), leading to a total duration of 10 s. The same thermal boundary conditions of the tensile loading case are applied, i.e. the bar (with initial temperature of 293 K) is thermally isolated and the temperature is prescribed at the two ends $\bar{T} = 293$K. The thermomechanical material properties are the same of the tensile loading case, which are presented in Table 3. To demonstrate the performance of the proposed algorithm under a variable time-step size, a trial time-step of $\Delta t = 0.5$s was chosen, which is adjusted by the $r_{\min}$ automatic time-step control technique.

The deformed configurations, at the end of the first stage (bar under traction forces) and at the end of the second stage (bar under compression forces), are presented in Fig. 19, showing the distribution of the equivalent plastic strain. There is a notorious change in the total length and radius of the bar as a consequence of the inversion on the loading path (tension to compression).

The evolution of the force applied to the cylindrical bar is presented in Fig. 20, where the two stages are separated for the sake of clarity. Thus, Fig. 20 (a) presents the first stage of the test (cylindrical bar under traction forces) and Fig. 20 (b) presents the second stage of the test (cylindrical bar under compression

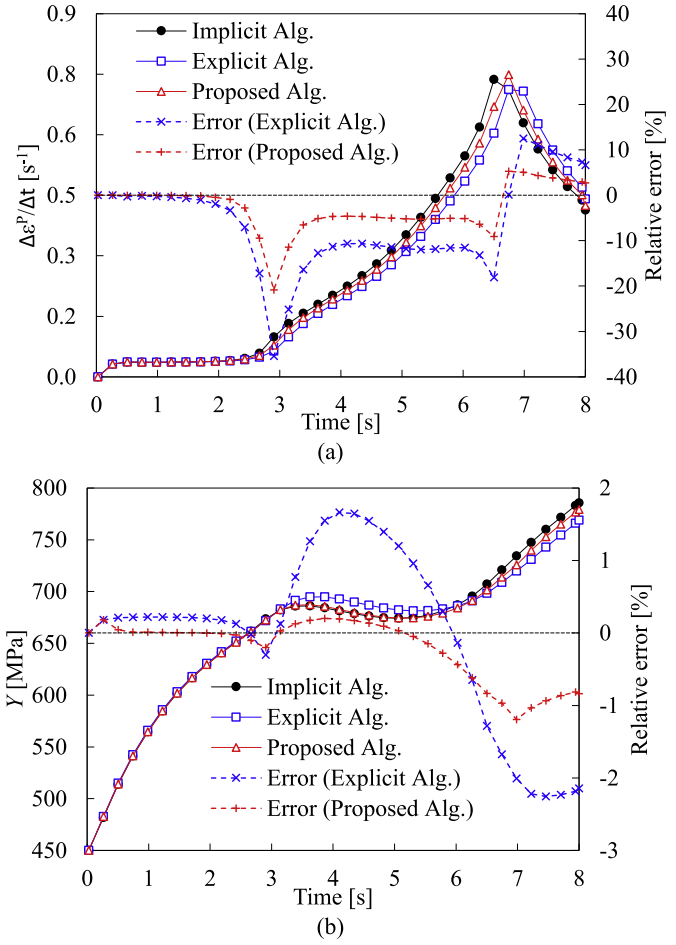

Fig. 18. Evolution of the: (a) equivalent plastic strain rate and (b) flow stress for the gauss integration point nearest to node A (see Fig. 12) using the different coupling algorithms and the relative error considering the implicit coupling strategy as a reference.

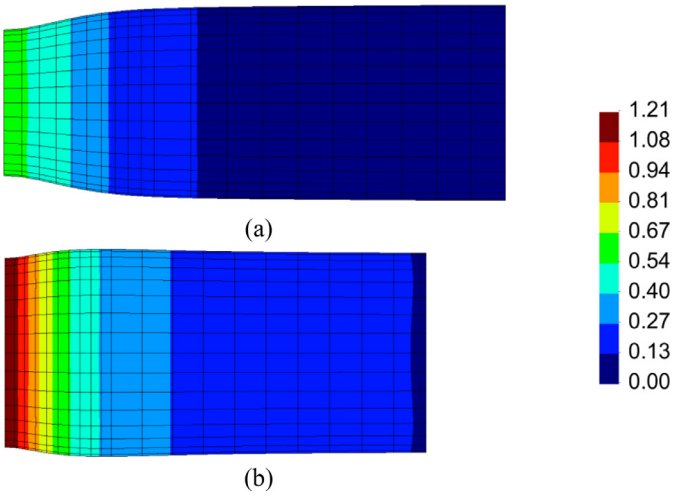

Fig. 19. Equivalent plastic strain plotted on the deformed configuration of the bar: (a) end of the tension stage ($t=5$ s); (b) end of the compression stage ($t=10$ s).

forces). To evaluate the influence of a non-constant time-step size on the results, another solution for the implicit algorithm is presented (green line), obtained with very small constant time-step $\Delta t=0.0005$s (labelled as $\times 0.0001$). Although not shown here, all algorithms lead to the same solution for this very small constant time-step (relative error in the temperature evolution for node A lower than 0.7% for the explicit algorithm and lower than 0.1% for the proposed one). Thus, this solution is assumed as the most accurate one and consequently, was used as a reference to calculate the relative error for the three algorithms. For the first stage (see Fig. 20 (a)) and until the onset of necking, the error of the implicit and of the proposed algorithms is almost zero, whereas the explicit algorithm presents a higher error. After the onset of necking, the error of both the implicit and the explicit algorithms tends to increase, although presenting different signs. On the other hand, the proposed algorithm maintains an almost constant error until the end of this stage. However, it should be mentioned that the prediction of the necking instability is sensitive to the time-step size selected. Moreover, the time-step size evolution also affects the results accuracy. In this context, the analysis of the relative error must be done carefully, since the conclusions are problem-specific, i.e. should not be generalized.

In the first time-step of the second stage, the error increases its magnitude for all algorithms (see Fig. 20 (b)). However, the proposed algorithm maintains a low value and converges for zero. The explicit and implicit algorithms have a higher error in the beginning of the second stage, but both converge to zero. These results show a dependence of the three algorithms on the time-step size. The explicit solution presents the higher magnitude of error, followed by the implicit algorithm which, despite the iterative cycle, has a worse solution than the proposed algorithm.

The relative temperature evolution in node A (see Fig. 12) is presented in Fig. 21. The error is also presented for three algorithms. Once again, the temperature rate has a significant increase after the necking. The error of the three algorithms is very close until the onset of necking, after that the explicit algorithm and the proposed algorithm underestimate the temperature, while the implicit algorithm overestimates it. After the inversion of the loading path, there is a drop in the temperature as a consequence of the elastic unloading. Since there is no heat generated by plastic deformation, the conduction effect dominates the thermal field during these instants. When the material begins to yield again, the temperature increases due to the heat generated by plastic deformation. A remark must be made concerning the behaviour of the proposed algorithm during the unloading, since in the prediction phase, the thermal problem is solved with the information of the previous increment. Accordingly, the predicted temperature field can be overestimated. This drawback of the proposed algorithm is mitigated by imposing a very small time-step in each change of stage. Fig. 22 shows the evolution of the time-step size for the three algorithms, highlighting that the $r_{\min}$ control technique, automatically reduces the time-step at the onset of necking and during the change of stage. Although all algorithms predict the maximum force for the same displacement, its magnitude is different (see Fig. 20 (a)) since there are also differences in the temperature field (see Fig. 21). At the onset of necking, the implicit algorithm requires the activation of the $r_{\min}$ strategy in the following time-steps, to avoid convergence problems in the mechanical solution. On the other hand, the explicit and the proposed algorithms perform one more time-step before the activation of the $r_{\min}$ strategy. This has an impact on the total number of increments required by the three algorithms, which also depends on the adjustment performed at the end, to guarantee the total time.

In conclusion, as expected the three algorithms are sensitive to the time-step size. Moreover, for this specific example, globally the error attained by the proposed algorithm is the lowest, for most of the test duration. In this context, it is important to remind that the implicit algorithm begins the correction phase with a solution for the temperature field corresponding to the equilibrium one for the previous increment, which is not correct and will be updated

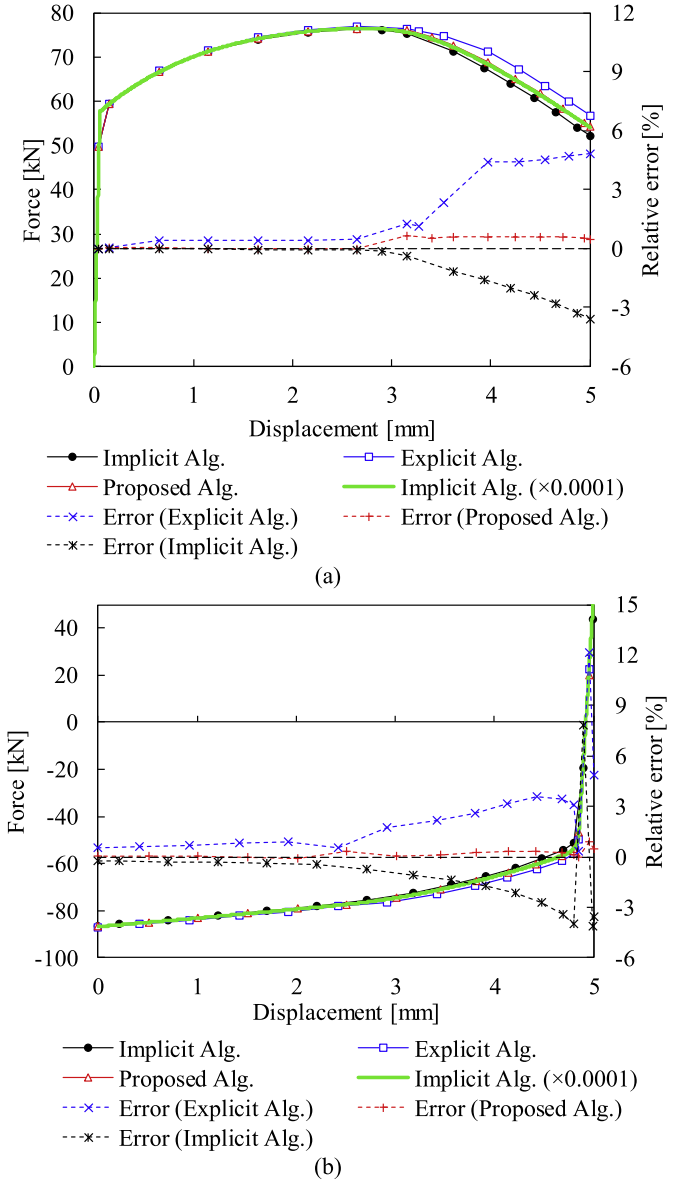

Fig. 20. Evolution of the force in the cylindrical bar obtained with different coupling algorithms and the relative error considering the solution obtained with the implicit coupling strategy with a constant small time-step as a reference. (a) first stage of the test (bar under traction forces) and (b) second stage of the test (bar under compression forces).

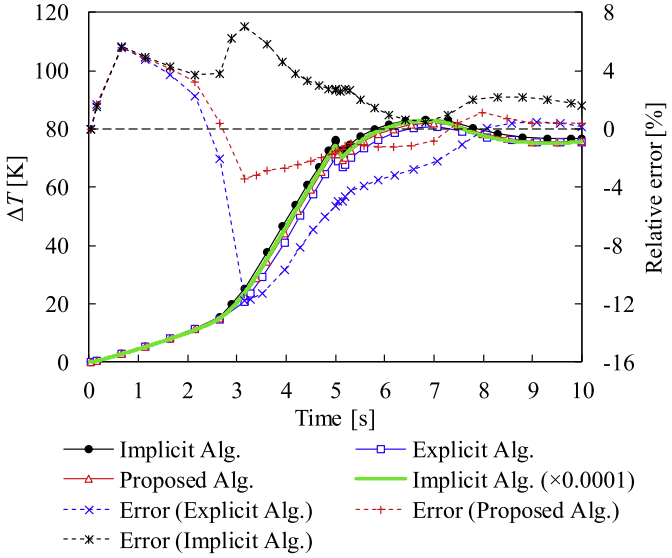

Fig. 21. Evolution of the relative temperature predicted in node A (see Fig. 12) using the different coupling algorithms and the relative error considering the solution obtained with the implicit coupling strategy with a constant small time-step as a reference.

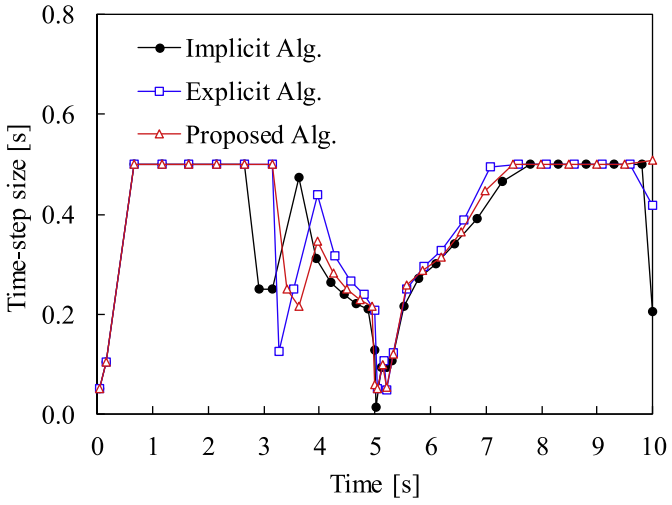

Fig. 22. Evolution of the time-step size for the three algorithms, implicit, explicit and proposed.

Table 5
Computational performance of the different coupling algorithms used in the cylindrical bar under tension-compression example.

	Implicit Alg.	Explicit Alg.	Proposed Alg.
Nº increments	32	30	31
CPU time [s]	281	92	96

within the iterative cycle. In the example under analysis, the error for the implicit solution increases after the onset of necking (see Fig. 20 (a) and Fig. 21), when the temperature rate increases. Despite the iterative cycle, due to this increase in the temperature, the initial solution dictates the accuracy of the final solution. Thus, it can be concluded that the prediction phase of the proposed algorithm plays an important role in the accuracy of the results.

The computational performance was evaluated based on the CPU time for the three algorithms and the results are presented in Table 5. The implicit algorithm needed 32 increments to complete the thermomechanical simulation, whereas the explicit and the proposed needed only 30 and 31, respectively. Such as in the first part of this example, the computational time required by the implicit algorithm is significantly higher than for the other two algorithms. This is the consequence of the iterative cycle which assures the equilibrium of the global thermomechanical problem at the end of the increment. Furthermore, the difference in the computational time between the explicit algorithm and the proposed algorithm are negligible, also when considering a non-constant time-step. Moreover, taking also the results accuracy into account, the proposed algorithm achieves better results than the explicit algorithm and its computational cost is similar to the one obtained with the explicit.

5. Conclusions

The design of staggered algorithms used in the solution of thermomechanical problems is still a current and challenging research topic in the field of computational mechanics. In this study a new

staggered algorithm for the thermomechanical coupling has been proposed, which considers the isothermal split. This algorithm was implemented in the in-house finite element code DD3IMP.

This new algorithm was designed with the purpose of creating a better compromise between computational cost and accuracy, based on classical algorithms presented in the literature, namely the explicit and the implicit. The proposed algorithm differs from the classics in the way the information is interchanged between the thermal and the mechanical problems. In contrast with the classical algorithms, the proposed algorithm has two distinct phases, the first one called prediction and the second one called correction. In both phases the mechanical and the thermal problem are solved sequentially. The prediction phase of this algorithm allows to improve the accuracy and to take advantage of automatic time-step control techniques, previously implemented for the mechanical problem.

Three numerical examples considering the heat generated by plastic deformation have been used to validate and assess the accuracy and computational efficiency of the proposed algorithm, namely the expansion of thermoplastic cylinder, the elementary uniaxial test and the necking of a circular bar with different loading conditions. A detailed comparison between the three algorithms was performed, as well as an evaluation of the influence of the time-step size. Variables such as temperature, equivalent von Mises stress and plastic strain rate have been assessed. The relative error in these variables, predicted with the explicit and the proposed algorithm, has been evaluated considering the implicit algorithm as reference. In each time-step, the delay between the mechanical and the thermal solutions obtained with the explicit staggered algorithm affects strongly the accuracy of the solution, but it can be improved by means of reducing the time-step size. Alternatively, for the same increment size, the proposed algorithm provides more accurate results in comparison with the explicit algorithm. Indeed, the relative error of the proposed algorithm is always at least half the value of error achieved with the explicit algorithm. This results from the trial temperature field determined in the prediction phase, which is evaluated assuming that the fraction of plastic power converted into heat is the same as for the previous increment. Concerning the computational cost, the proposed algorithm retains the characteristic low computational cost of the explicit algorithm, which is half of the implicit algorithm for the examples analysed.

Acknowledgments

The authors gratefully acknowledge the financial support of the Portuguese Foundation for Science and Technology (FCT) under projects P2020-PTDC/EMS-TEC/0702/2014 (POCI-01-0145-FEDER-016779) and P2020-PTDC/EMS-TEC/6400/2014 (POCI-01-0145-FEDER-016876) by UE/FEDER through the program COMPETE 2020. The second author is also grateful to the FCT for the Post-doctoral grant SFRH/BPD/101334/2014.

References

Adam, L., Ponthot, J., 2002. Numerical simulation of viscoplastic and frictional heating during finite deformation of metal. part I. Theory. J. Eng. Mech. 128 (1), 1222–1232. doi:10.1061/(ASCE)0733-9399(2002)128:11(1222).

Adam, L., Ponthot, J.P., 2005. Thermomechanical modeling of metals at finite strains: First and mixed order finite elements. Int. J. Solids Struct. 42, 5615–5655. doi:10.1016/j.ijsolstr.2005.03.020.

Agelet De Saracibar, C., Cervera, M., Chiumenti, M., 1999. On the formulation of coupled thermoplastic problems with phase-change. Int. J. Plast. 15, 1–34. doi:10.1016/S0749-6419(98)00055-2.

Akbari, M., Buhl, S., Leinenbach, C., Wegener, K., 2016. A new value for Johnson–Cook damage limit criterion in machining with large negative rake angle as basis for understanding of grinding. J. Mater. Process. Technol. 234, 58–71. doi:10.1016/j.jmatprotec.2016.03.009.

Alves, J.L., 2003. Simulação Numérica Do Processo De Estampagem De Chapas metálicas: Modelação Mecânica e Métodos Numéricos. University of Minho.

Andrade-Campos, A., da Silva, F., Teixeira-Dias, F., 2007. Modelling and numerical analysis of heat treatments on aluminium parts. Int. J. Numer. Methods Eng. 70, 582–609. doi:10.1002/nme.1905.

Andrade-Campos, A., Menezes, L.F., Teixeira-Dias, F., 2006. Numerical analysis of large deformation processes at elevated temperatures. Comput. Methods Appl. Mech. Eng. 195, 3947–3959. doi:10.1016/j.cma.2005.07.023.

Argyris, J.H., Doltsinis, J.S., 1981. On the natural formulation and analysis of large deformation coupled thermomechanical problems. Comput. Methods Appl. Mech. Eng. 25, 195–253. doi:10.1016/0045-7825(81)90084-0.

Argyris, J.H., Vaz, L.E., Willam, K.J., 1981. Integrated finite-element analysis of coupled thermoviscoplastic problems. J. Therm. Stress. 4, 121–153. doi:10.1080/01495738108909960.

Armero, F., Simo, J.C., 1992. A new unconditionally stable fractional step method for non-linear coupled thermomechanical problems. Int. J. Numer. Methods Eng. 35, 737–766. doi:10.1002/nme.1620350408.

Armero, F., Simo, J.C., 1993. A priori stability estimates and unconditionally stable product formula algorithms for nonlinear coupled thermoplasticity. Int. J. Plast. 9, 749–782. doi:10.1016/0749-6419(93)90036-P.

Barros, P.D., Alves, J.L., Oliveira, M.C., Menezes, L.F., 2016. Modeling of tension–compression asymmetry and orthotropy on metallic materials: Numerical implementation and validation. Int. J. Mech. Sci. 114, 217–232. doi:10.1016/j.ijmecsci.2016.05.020.

Bathe, K.-J., Bouzinov, P.A., Pantuso, D., 2000. A finite element procedure for the analysis of thermo- mechanical solids in contact. Comput. Struct. 75, 551–573. doi:10.1016/S0045-7949(99)00212-6.

Bathe, K.J., 1996. Finite Element Procedures. Prentice-Hall, Englewood Cliffs.

Bever, M.B., Holt, D.L., Titchener, A.L., 1973. The stored energy of cold work. Prog. Mater. Sci. 17, 5–177. doi:10.1016/0079-6425(73)90001-7.

Canadija, M., Brnic, J., 2004. Associative coupled thermoplasticity at finite strain with temperature-dependent material parameters. Int. J. Plast. 20, 1851–1874. doi:10.1016/j.ijplas.2003.11.016.

Cervera, M., Codina, R., Galindo, M., 1996. On the computational efficiency and implementation of block-iterative algorithms for nonlinear coupled problems. Eng. Comput. 13, 4–30. doi:10.1108/02644409610128382.

Danowski, C., Gravemeier, V., Yoshihara, L., Wall, W.A., 2013. A monolithic computational approach to thermo-structure interaction. Int. J. Numer. Methods Eng. 95, 1053–1078. doi:10.1002/nme.4530.

Dunić, V., Busarac, N., Slavković, V., Rosić, B., Niekamp, R., Matthies, H., Slavković, R., Živković, M., 2016. A thermo-mechanically coupled finite strain model considering inelastic heat generation. Contin. Mech. Thermodynamics 28, 993–1007. doi:10.1007/s00161-015-0442-5.

Erbts, P., Düster, A., 2012. Accelerated staggered coupling schemes for problems of thermoelasticity at finite strains. Comput. Math. with Appl. 64, 2408–2430. doi:10.1016/j.camwa.2012.05.010.

Fekete, B., Szekeres, A., 2015. Solids investigation on partition of plastic work converted to heat during plastic deformation for reactor steels based on inverse experimental-computational method Eur. J. Mech. A 53, 175–186.

Felippa, C.A., Park, K.C., Farhat, C., 2001. Partitioned analysis of coupled mechanical systems. Comput. Methods Appl. Mech. Eng. 190, 3247–3270. doi:10.1016/S0045-7825(00)00391-1.

Håkansson, P., Wallin, M., Ristinmaa, M., 2005. Comparison of isotropic hardening and kinematic hardening in thermoplasticity. Int. J. Plast. 21, 1435–1460. doi:10.1016/j.ijplas.2004.07.002.

Hughes, T.J.R., 1980. Generalization of selective integration procedures to anisotropic and nonlinear media. Int. J. Numer. Methods Eng. 15, 1413–1418. doi:10.1002/nme.1620150914.

Ibrahimbegovic, A., Chorfi, L., 2002. Covariant principal axis formulation of associated coupled thermoplasticity at finite strains and its numerical implementation. Int. J. Solids Struct. 39, 499–528. doi:10.1016/S0020-7683(01)00221-9.

Karbasian, H., Tekkaya, A.E., 2010. A review on hot stamping. J. Mater. Process. Technol. 210, 2103–2118. doi:10.1016/j.jmatprotec.2010.07.019.

Kleiber, M., 1991. Computational coupled non-associative thermo-plasticity. Comput. Methods Appl. Mech. Eng. 90, 943–967. doi:10.1016/0045-7825(91)90192-9.

Laurent, H., Coër, J., Manach, P.Y., Oliveira, M.C., Menezes, L.F., 2015. Experimental and numerical studies on the warm deep drawing of an Al–Mg alloy. Int. J. Mech. Sci. 93, 59–72. doi:10.1016/j.ijmecsci.2015.01.009.

Lee, E.H., Yang, D.Y., Yoon, J.W., Yang, W.H., 2015. Numerical modeling and analysis for forming process of dual-phase 980 steel exposed to infrared local heating. Int. J. Solids Struct. 75–76, 211–224. doi:10.1016/j.ijsolstr.2015.08.014.

Li, D.Y., Chen, Z., Sun, L., Lee, J.W., Wagoner, R.H., 2016. An improved test for shear fracture. Int. J. Solids Struct. 97, 29–42. doi:10.1016/j.ijsolstr.2016.08.002.

Martins, J.M.P., Alves, J.L., Neto, D.M., Oliveira, M.C., Menezes, L.F., 2016a. Numerical analysis of different heating systems for warm sheet metal forming. Int. J. Adv. Manuf. Technol. 83, 897–909. doi:10.1007/s00170-015-7618-9.

Martins, J.M.P., Alves, J.L., Neto, D.M., Oliveira, M.C., Menezes, L.F., 2016b. Numerical modeling of the thermal contact in metal forming processes. Int. J. Adv. Manuf. Technol. 87, 1797–1811. doi:10.1007/s00170-016-8571-y.

Matthies, H.G., Niekamp, R., Steindorf, J., 2006. Algorithms for strong coupling procedures. Comput. Methods Appl. Mech. Eng. 195, 2028–2049. doi:10.1016/j.cma.2004.11.032.

Menezes, L.F., Teodosiu, C., 2000. Three-dimensional numerical simulation of the deep-drawing process using solid finite elements. J. Mater. Process. Technol. 97, 100–106. doi:10.1016/S0924-0136(99)00345-3.

Neto, D.M., Coër, J., Oliveira, M.C., Alves, J.L., Manach, P.Y., Menezes, L.F., 2016. Numerical analysis on the elastic deformation of the tools in sheet metal forming processes. Int. J. Solids Struct. 100–101, 270–285. doi:10.1016/j.ijsolstr.2016.08.023.

Neto, D.M., Oliveira, M.C., Menezes, L.F., Alves, J.L., 2015. A contact smoothing method for arbitrary surface meshes using Nagata patches. Comput. Methods Appl. Mech. Eng. 299, 283–315. doi:10.1016/j.cma.2015.11.011.

Netz, T., Hartmann, S., 2015. A monolithic finite element approach using high-order schemes in time and space applied to finite strain thermo-viscoelasticity. Comput. Math. Appl. 70, 1457–1480. doi:10.1016/j.camwa.2015.03.030.

Neugebauer, R., Altan, T., Geiger, M., Kleiner, M., Sterzing, A., 2006. Sheet metal forming at elevated temperatures. CIRP Ann. - Manuf. Technol. 55, 793–816. doi:10.1016/j.cirp.2006.10.008.

Novascone, S.R., Spencer, B.W., Hales, J.D., Williamson, R.L., 2015. Evaluation of coupling approaches for thermomechanical simulations. Nucl. Eng. Des. 295, 910–921. doi:10.1016/j.nucengdes.2015.07.005.

Oliveira, M.C., Alves, J.L., Menezes, L.F., 2008. Algorithms and strategies for treatment of large deformation frictional contact in the numerical simulation of deep drawing process. Arch. Comput. Methods Eng. 15, 113–162. doi:10.1007/s11831-008-9018-x.

Oliveira, M.C., Menezes, L.F., 2004. Automatic correction of the time step in implicit simulations of the stamping process. Finite Elem. Anal. Des. 40, 1995–2010. doi:10.1016/j.finel.2004.01.009.

Pereira, M.P., Rolfe, B.F., 2014. Temperature conditions during “cold” sheet metal stamping. J. Mater. Process. Technol. 214, 1749–1758. doi:10.1016/j.jmatprotec.2014.03.020.

Ponthot, J.-P., Papeleux, L., 2014. Thermoviscoplasticity at finite strains: a thermoelastic predictor–viscoplastic corrector algorithm. In: Encyclopedia of Thermal Stresses. Springer, Netherlands, Dordrecht, pp. 6092–6105. doi:10.1007/978-94-007-2739-7_674.

Rahman Chukkan, J., Vasudevan, M., Muthukumaran, S., Ravi Kumar, R., Chandrasekhar, N., 2015. Simulation of laser butt welding of AISI 316 L stainless steel sheet using various heat sources and experimental validation. J. Mater. Process. Technol. 219, 48–59. doi:10.1016/j.jmatprotec.2014.12.008.

Ristinmaa, M., Wallin, M., Ottosen, N.S., 2007. Thermodynamic format and heat generation of isotropic hardening plasticity. Acta Mech 194, 103–121. doi:10.1007/s00707-007-0448-6.

Rothe, S., Erbts, P., Düster, A., Hartmann, S., 2015. Monolithic and partitioned coupling schemes for thermo-viscoplasticity. Comput. Methods Appl. Mech. Eng. 293, 375–410. doi:10.1016/j.cma.2015.05.002.

Simo, J.C., Miehe, C., 1992. Associative coupled thermoplasticity at finite strains: formulation, numerical analysis and implementation. Comput. Methods Appl. Mech. Eng. 98, 41–104. doi:10.1016/0045-7825(92)90170-O.

Taylor, G.I., Quinney, H., 1934. The latent energy remaining in a metal after cold working. Proc. R. Soc. A Math. Phys. Eng. Sci. 143, 307–326. doi:10.1098/rspa.1934.0004.

Ulz, M.H., 2009. A Green–Naghdi approach to finite anisotropic rate-independent and rate-dependent thermo-plasticity in logarithmic Lagrangean strain-entropy space. Comput. Methods Appl. Mech. Eng. 198, 3262–3277. doi:10.1016/j.cma.2009.06.006.

Vaz, M., Muñoz-Rojas, P.A., Lange, M.R., 2011. Damage evolution and thermal coupled effects in inelastic solids. Int. J. Mech. Sci. 53, 387–398. doi:10.1016/j.ijmecsci.2011.03.001.

Wriggers, P., Miehe, C., Kleiber, M., Simo, J.C., 1992. On the coupled thermomechanical treatment of necking problems via finite element methods. Int. J. Numer. Methods Eng. 33, 869–883. doi:10.1002/nme.1620330413.

Xing, H.L., Makinouchi, A., 2002a. Three dimensional finite element modeling of thermomechanical frictional contact between finite deformation bodies using R-minimum strategy. Comput. Methods Appl. Mech. Eng. 191, 4193–4214. doi:10.1016/S0045-7825(02)00372-9.

Xing, H.L., Makinouchi, a., 2002b. FE modeling of thermo-elasto-plastic finite deformation and its application in sheet warm forming. Eng. Comput. 19, 392–410. doi:10.1108/02644400210430172.

Yamada, Y., Yoshimura, N., Sakurai, T., 1968. Plastic stress-strain matrix and its application for the solution of elastic-plastic problems by the finite element method. Int. J. Mech. Sci. 10, 343–354. doi:10.1016/0020-7403(68)90001-5.